Journal of Manufacturing Processes 121 (2024) 100–120

Contents lists available at ScienceDirect

Journal of Manufacturing Processes

journal homepage: www.elsevier.com/locate/manpro

Enhanced joining strength in additive-manufactured polylactic-acid structures fused by embedded heated metallic meshes

Dongyang Cao, Dan Bouzolin, Hongbing Lu, D. Todd Griffith *

Department of Mechanical Engineering, The University of Texas at Dallas, Richardson, TX 75080, USA

ARTICLE INFO

Keywords:
Resistance welding
Fusion joining
Additive manufacturing
Thermoplastic polymer
Green manufacturing
Sustainability

ABSTRACT

Additively manufactured thermoplastic polymers, such as polylactic acid (PLA), hold significant promise for sustainable engineering structures, including wind turbine blades. Upscaling these structures beyond the limitations of 3D printer build volumes is a challenge; fusion joining presents a potential solution. This paper introduces a displacement-controlled resistance welding process for PLA, as an alternative to the typical force-controlled methods. We investigated the bonding quality of resistance-welded and adhesive-bonded PLA beams through three-point bending and measured the surface deformations using digital image correlation. Different metal meshes (30 %/0.11 mm Ni—Cu, 34 %/0.07 mm Ni—Cu, and 36 %/0.25 mm Co—Ni) served as heating elements. The process parameters were varied for the 34 %/0.07 mm Ni—Cu mesh to identify an optimum set of parameters. Results showed that this optimized displacement-controlled welding achieved 94 % of the original strength of monolithic samples. This indicates that the new welding process not only ensures high-quality bonding and fine surface finishing but also promotes sustainability, recyclability, and economic efficiency in various polymer and composite structural applications.

1. Introduction

The increasing adoption of additive manufacturing for making thermoplastic engineering structures, such as wind turbine blades, is driven by their cost-effectiveness, topological flexibility, and recyclability [1]. However, significant technical challenges in additively manufactured thermoplastic polymer structures must be addressed to fully realize their potential. Despite these challenges, thermoplastic polymers are emerging as a preferable alternative to commonly used thermoset polymers, primarily due to the environmental concerns associated with plastic pollution.

Plastic pollution, largely attributed to thermoset polymers, has irreversible environmental impacts, affecting carbon and nutrient cycles, aquatic ecosystems, and leading to ecotoxicity [1]. Borrelle et al. estimated that globally, 19 to 23 million tons of plastic waste were generated in 2016, and the figure is projected to rise to 53 million tons by 2030 [2]. In the US, approximately 77 % of plastic waste ends up in landfills, with only 6.2 % being recycled [3]. Recycling emerges as a crucial strategy in plastic waste management. Kazemi et al. indicated that selecting appropriate recycling methods can significantly reduce plastic waste [4]. However, chemical recycling methods, which often require large amounts of solvents, are both uneconomical and environmentally detrimental [5]. Mechanical recycling currently stands as the most practical approach for managing large volumes of plastic waste across various industries [6].

In various sectors of industries utilizing additive manufacturing, material selection is increasingly governed by a combination of traditional and emerging criteria. While mechanical properties continue to be essential, aspects such as manufacturability, sustainability, and recyclability are gaining prominence in decision-making processes. Polylactic acid (PLA) stands out due to its compatibility with additive manufacturing processes, cost-effectiveness, sustainability, and environmental benefits. Looking ahead, polyethylene terephthalate (PET) is poised to attract more attention, especially given the recent focus by researchers on their chemical recycling and upcycling efficiency [7]. Table 1 offers a comparison to provide a clear understanding of these materials in the context of 3D printing.

The use of polylactic acid (PLA) in additive manufacturing (AM) has seen a significant increase in recent years, primarily driven by its advantageous manufacturing processes, cost efficiency, and performance in material extrusion AM [23–25]. This trend in PLA usage is part of a larger movement in AM, where the incorporation of various polymers,

* Corresponding author.
E-mail address: tgriffith@utdallas.edu (D.T. Griffith).

https://doi.org/10.1016/j.jmapro.2024.04.089
Received 5 August 2023; Received in revised form 6 February 2024; Accepted 30 April 2024
Available online 18 May 2024

Table 1
A review of sustainability and recyclability of 3D printable materials. (References: Fonseca et al. [8], Liu et al. [9], Södergård et al. [10], Guo et al. [11], Pinto et al. [12], Ügdüler et al. [13], Bedell et al. [14], Teotia et al. [15], Rahimi et al. [16], Bai et al. [17], Su et al. [18], Sunil et al. [19], Olifirov et al. [20], Wölfel et al. [21], Abbasian et al. [22].)

Material (bulk)	Manufacture process	Tensile strength (mPa)	Glass transition temperature (°C)	Biodegradable	Recycling strategy	Recycling process	Sustainability	Advantage	Disadvantage
PLA	FDM	50–70	50–65	Yes	Mechanical	Crush, smash, and milling	89.7 % (1st) 91.1 % (2nd) 63.0 % (3rd)	Low melting temperature, biodegradable, low cost, ease to print	Low-impact strength, low-temperature application
ABS	FDM	~43	~105	No	Mechanical	Crush, smash, and milling	50 % (1st) 42 % (2nd) 29 % (3rd)	Thermally stable, high hardness/ impact strength	Low sustainability
Polyamide-6	FDM	~66.5	70–80	No	Mechanical	Crush, smash, and milling	96.9 % (5th) 70.9 % (10th) 46.9 % (15th)	High sustainability, high durability	High moister absorption, high shrinkage
PVC	FDM	34–62	~82	No	Mechanical	Crush, smash, and milling	37.1 % (1st)	Chemical stable, low cost, high insulation	Hard to print, low-temperature application, low sustainability
Polyimide	DLP	110–150	~230	No	Mechanical	Milling (Major application for nano-pellet)	–	Thermal/chemical stable, superior mechanical properties	Limited application after recycled, high energy consumption for resistance welding
PET	FDM	55–75	~80	No	Chemical/ Mechanical	Glycolysis, Hydrolysis, Alcoholysis, Aminolysis	100 %	High sustainability, low cost	Low heat resistance
TPU	FDM	~26	~65	YES	Mechanical	Crush, smash, and milling	95.5 % (1st) 86.4 % (4th) 81.8 % (8th)	High sustainability, low melting temperature, biodegradable	Poor mechanical properties, low-temperature application
Nomex	Adhesive Bonding	~340	–	No	Landfill, incineration	–	–	Thermal/chemical stable, good mechanical properties	Not 3D printable, low sustainability and recyclability
Resin Infused Balsa Wood	VARTM	10–20	–	No	Landfill, incineration	–	–	Thermal/chemical stable, good shear properties	Not 3D printable, low sustainability and recyclability

including thermoplastics, thermoset polymers, and elastomers, is becoming increasingly prevalent. Particularly notable is their application in Digital Light Processor (DLP) processes, which is expected to further expand the use of polymers in AM. This expansion is set to transform AM technologies, enabling more versatile, efficient production of a wide range of components, from prototypes to custom-made items [26–30]. These developments underscore the evolving nature of AM processes and their growing impact on manufacturing and design industries.

Although material extrusion processes in additive manufacturing (AM) offer advantages, they are not without limitations [31]. One significant challenge is that materials produced through this method typically exhibit lower strengths compared to their injection-molded counterparts, as noted in studies by Li et al. [32] and Duty et al. [33] Additionally, the size of components is constrained by the build volume of the material extrusion systems, which are generally $<150 \times 150 \times 150$ mm^3 for universal desktop printers and $800 \times 800 \times 800$ mm^3 for industrial printers. However, there are exceptions, such as the University of Maine's large-scale 3D printer, boasting a build volume of $30.48 \times 6.71 \times 3.05$ m^3. This printer was used to fabricate the world's largest 3D printed boat, '3Dirigo' [34]. Large-scale 3D printed structures are increasingly employed as core components in various fields, including aeronautics, road vehicles, ships, and civil engineering [35–37].

In this joining method, a critical issue that must be resolved is developing effective methods for joining these parts while ensuring satisfactory bonding quality and mechanical performance. This paper focuses on addressing this specific issue, with an intention to advance the capabilities of AM in producing larger, structurally sound components for diverse applications.

To manufacture large-size parts in additive manufacturing, a variety of methods are employed to join thermoplastic parts produced through material extrusion. Mechanical fastening, such as interlocking mechanisms akin to joining Lego parts, offers a straightforward approach. Adhesive bonding, particularly using epoxy adhesives, is favored for its simplicity. However, a significant drawback is that most commercial epoxy adhesives are not specifically formulated for 3D printable thermoplastic polymers [38–40], indicating a need for more tailored adhesive solutions in this field.

In various fusion joining techniques, several methods present viable alternatives for assembling thermoplastic components. These include infrared welding, induction welding, ultrasonic welding, resistance welding, and laser welding, each offering unique benefits in terms of bonding strength and precision [38,41]. Recently, friction stir welding and friction spinning have also emerged as popular methods for joining additively manufactured parts, adding to the arsenal of available techniques in the industry.

Despite the variety of available methods, to the best of our knowledge, resistance welding has not been extensively explored for the fusion joining of additively manufactured thermoplastic polymer parts. This paper will fill this gap by investigating the application of resistance

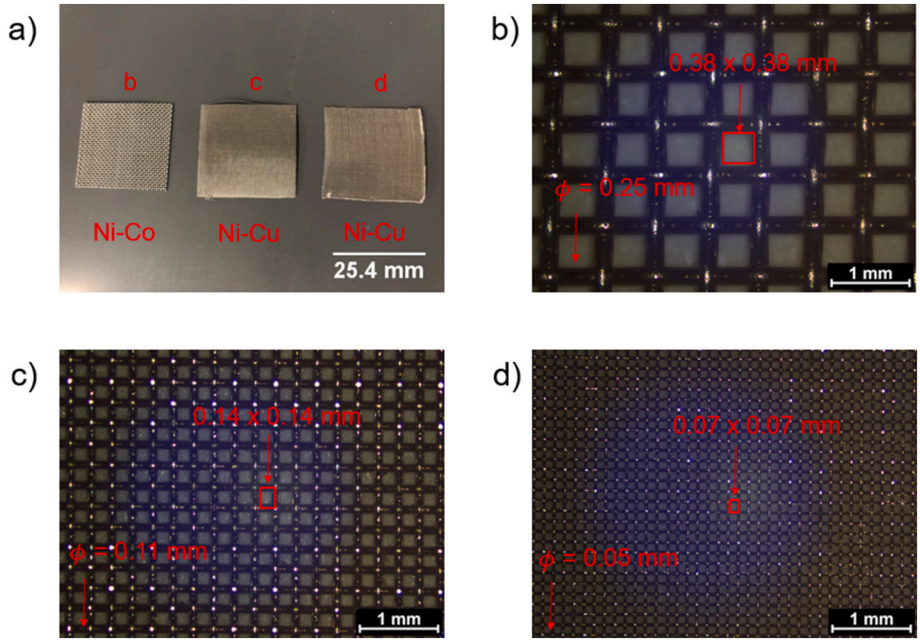

Fig. 1. Microscopic images captured using a Leica DMI 8 microscope, showing three types of metal meshes. a) Overview of 25.4 × 25.4 mm mesh samples, representing all three types of metal meshes; b) close-up of the 36 %/0.25 mm Ni-Co metal mesh, highlighting its structural details; c) detailed view of the 30 %/0.11 mm Ni-Cu metal mesh, illustrating its specific configuration; d) magnified image of the 34 %/0.07 mm Ni-Cu metal mesh, focusing on its unique characteristics.

welding in this context. Our study seeks to understand its effectiveness and potential advantages over other methods, thereby contributing to the advancement of joining technologies in the field of additive manufacturing.

Resistance welding, a widely used technique for joining thermoplastic polymer matrix fiber-reinforced composites, has been the focus of various studies. This process, commonly applied to composites such as graphite (G), carbon fibers (CF), and glass fibers (GF) in matrix materials such as PE, PP, PET, PEI, PPS, PEEK, and Elium 188, typically utilizes a force-controlled welding approach. Heating elements in these studies have included unidirectional (UD) carbon fiber prepreg, carbon fiber fabric, stainless steel mesh, and CNT embedded in PP film, with bonding quality assessed via lap shear strength testing [42].

Eveno et al., reported a lap shear strength of 31 MPa for CF/PEI composites using a unidirectional CF/PEI heating element under specific conditions [43]. Similarly, Warren et al. found that GF/PET composites, when resistance welded with stainless steel mesh, achieved a lap shear strength of 25.4 MPa [44]. Dube et al. highlighted the effectiveness of stainless steel mesh in achieving higher lap shear strengths in various composites, including CF/PEEK, CF/PER, and GF/PEI [45]. Russello et al. demonstrated the potential of CNT film in resistance welding of PEEK polymers, achieving 96 % of the strength of continuous PEEK polymer [46]. Murray et al. explored various heating elements with GF/Elium 188 composites, finding significant differences in lap shear strengths depending on the heating element used [47].

Additionally, Choudhury et al. investigated bamboo fiber/PLA composites, revealing that those resistance welded parts with carbon fiber fabric heating elements exhibited significantly higher tensile and compressive strengths compared to those using stainless steel mesh and PP film [48]. These studies collectively highlight the diverse applications of resistance welding in thermoplastic composites and point towards the continual optimization of this process for various material combinations.

Compared to the pressure-controlled method, the displacement-controlled method in resistance welding offers key advantages, particularly in reducing the likelihood of over-squeezed flow in the polymer bonding region. This approach also allows for more precise control over the final geometry of the finished part, a critical aspect for many applications. Regarding heating elements, carbon fibers and stainless steel mesh have been predominantly investigated. However, carbon fiber elements face challenges due to the high melting viscosity of 3D printed polymers, which complicates full impregnation and wetting of the fibers [49]. Additionally, while unidirectional carbon prepreg is commonly used, it often results in nonuniform heat distribution [50,51].

On the other hand, stainless steel mesh tends to provide more uniform current flow and effective polymer impregnation due to its consistent wire resistance and larger open area, leading to improved bonding quality [52]. Dube et al. have highlighted that the mesh opening fraction and wire diameter ratio significantly affect bonding quality [45]. However, stainless steel mesh is not without issues, as it can cause current leakage due to high current induction.

In our work, we address these challenges by exploring three new types of heating elements. These elements are designed to mitigate the limitations observed in traditional materials and improve the overall efficiency and quality of the resistance welding process.

This paper investigates the bonding quality of additively-manufactured PLA polymers resistance welded using Ni/Cu and Ni/Co metal meshes, employing a displacement-controlled process – a method not extensively studied previously. We focused on understanding the bonding mechanism between the metal mesh and 3D printed parts in this context. Our study involved measuring the flexural strength and modulus of slender samples with four types of infill patterns. Multiple 13.97 × 76.2 × 76.2 mm samples were printed using material extrusion and subsequently joined via resistance welding. We evaluated the bonding quality through microscopy, digital image correlation, and three-point bending tests.

A novel aspect of our study was the characterization of the mode I fracture (opening crack) behavior under three-point bending tests as a performance metric, instead of the conventional mode II fracture (shear crack) in lap shear tests. This approach was adopted to address the issue of PLA build layer interface fracture prior to bond line fracture. Additionally, we conducted multivariable linear regression analysis to uncover correlations between the parameters of displacement-controlled resistance welding and welding strength efficiency. The first principal strain distributions in the welded samples under bending were determined using the digital image correlation (DIC) technique. A discussion

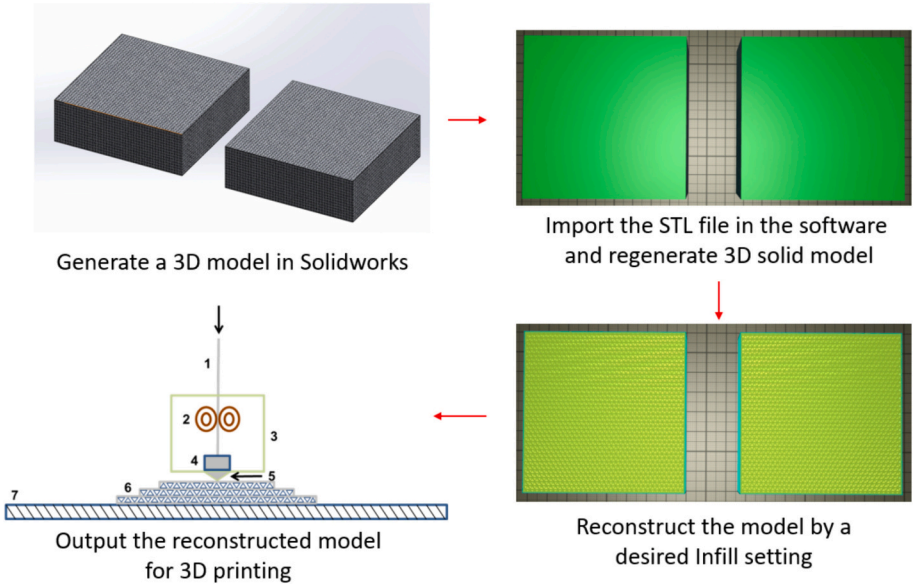

Fig. 2. Schematic of the 3D printing (material extrusion) process. This illustration shows the key components of the 3D printer, including 1) the 3D printing filament; 2) the filament feeding roller; 3) the 3D printing head, which guides the filament; 4) the hot-end, where the filament is melted; 5) the stainless steel nozzle, through which the molten filament is extruded; 6) the 3D printed parts; and 7) the Kapton coated 3D printing platform, providing the base on which the parts are printed.

is provided to summarize the advantages and drawbacks of each fusion joining process investigated herein, providing valuable insights into the efficacy and applicability of these methods in additive manufacturing.

2. Experimental methods

This section describes the procedures used in the preparation of 3D-printed samples, along with a detailed description of the experimental methods used to characterize their mechanical properties. It includes specifics on the printing processes, material selection, and post-processing steps, as well as the methodologies and instruments utilized in the mechanical testing of these samples.

2.1. Materials

PLA filaments from Craftbot (Carrollton, TX), with a diameter of 1.75 mm, were selected as the 3D printing material due to their favorable strength-to-weight ratio and lower printing temperature compared to other materials [53]. For the heating element in the resistance welding of these 3D-printed PLA samples, Ni—Co metal alloy meshes from McMaster-Carr (Elmhurst, IL) were used. These meshes, featuring an opening size of 0.381 mm, a 36 % open area fraction, and a wire diameter of 0.25 mm, can reach a maximum temperature of 982 °C [54]. The choice of these meshes was made by the consideration of their effective impregnation capabilities and efficiency in temperature generation, attributed to their low wire diameter and constant open area.

Two types of Ni—Cu metal alloy mesh, also from McMaster-Carr, were employed for comparison. The first type has an opening size of 0.07 mm, a 34 % open area fraction, and a wire diameter of 0.05 mm. The second type has an opening size of 0.14 mm, a 30 % open area fraction, and a wire diameter of 0.11 mm. Fig. 1 shows these metal meshes under microscopy. According to Dube et al. [45], all three mesh types are capable of achieving high bonding quality due to their favorable ratio of open area fraction to wire diameter. These meshes were also selected for their corrosion resistance, thermal oxidation resistance, and superior thermal efficiency compared to stainless steel meshes.

As a benchmark, Plexus MA310 high-strength MMA adhesives from Perigee Direct (North Richland Hills, TX) were used for adhesive bonding of the PLA specimens. This adhesive was chosen for its higher strength relative to other brands, particularly for bonding thermoplastic polymer matrices [47].

2.2. Fabrication of additive-manufactured three-point bending specimens

A schematic of the material extrusion process utilized in this study is illustrated in Fig. 2. The samples were printed using a Craftbot 3 dual extrusion 3D printer (Craftbot, Carrollton, TX), which has a total build volume of 250 × 200 × 200 mm. This printer can operate within a temperature range of 20–300 °C and reach a maximum printing speed of 200 mm/s [55]. The first step in the printing process involved creating the sample's geometry in AutoCAD or Solidworks and exporting it as an STL file. This file was then imported into CraftWarePRO (Craftbot, Carrollton, TX), where the 3D print settings were carefully adjusted.

For our experiments, the printing speed was set to 38 mm/s, and the travel speed to 57 mm/s. We used a stainless-steel nozzle with a diameter of 0.4 mm and set the print layer height to 0.3 mm to ensure a smooth surface finish on the samples. The temperatures for the nozzle and bed were set to 215 °C and 60 °C, respectively. The infill density was chosen as 40 %, with an infill angle and increment angle of 0 degree for each layer to optimize sample stiffness. Additionally, a raft was added beneath each sample to enhance adhesion to the print bed. Multiple infill patterns were tested to evaluate their impact on sample stiffness. To ensure consistent print quality, a nozzle-to-bed level calibration and a preheat of the nozzle and bed were performed before each printing session to prevent nozzle clogging.

2.3. Fabrication of slender beam specimens via resistance welding

The setup for the resistance welding process is depicted in Fig. 3. This section will describe the specific procedures involved in resistance welding. Initially, the welding areas, measuring 13.97 mm × 76.2 mm, were meticulously cleaned with 75 % ethanol. This step is crucial for removing contaminants and ensuring optimal bonding quality. After cleaning, a metal alloy mesh (either Ni—Co or Ni—Cu) was positioned between the 3D printed parts. To complete the setup, two copper electrode wires, each 90 mm in length, were connected to the mesh to maintain consistent wire resistance.

For the application of uniform pressure and controlled displacement during welding, we employed a Model 5969 Instron universal testing system (Instron, Norwood, MA) along with compression platens. The

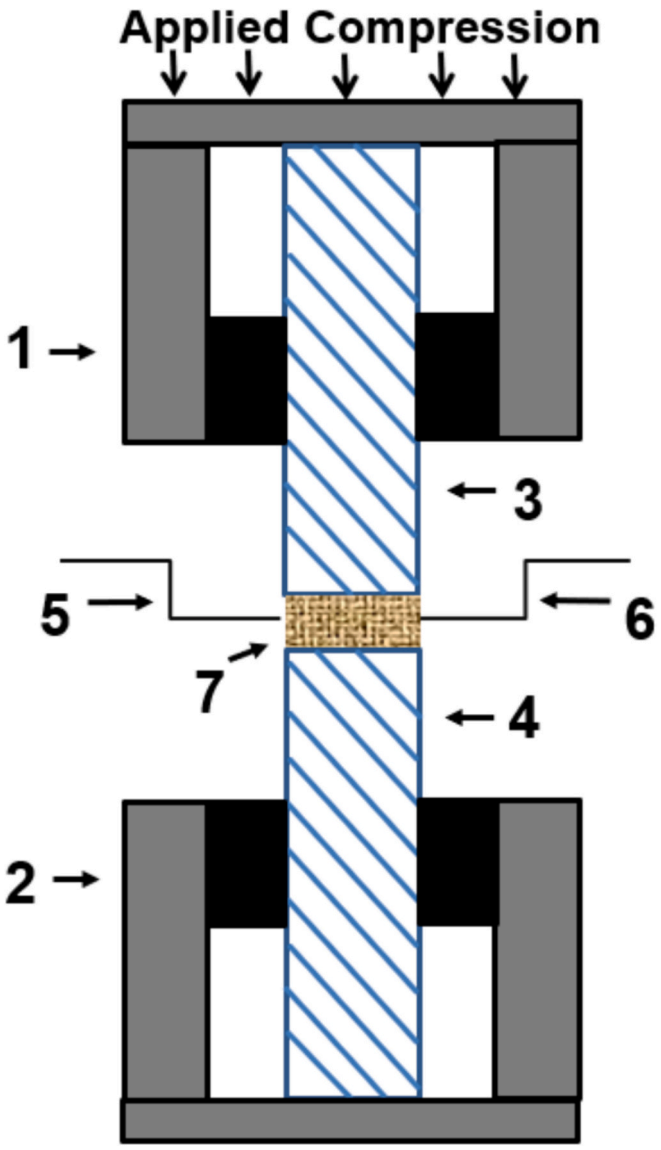

Fig. 3. Schematic of the resistance welding setup; 1 & 2: compression platens; 3 & 4: PLA thermoplastic polymer block; 5 & 6: copper metal wire; 7: metal alloy mesh.

heat necessary for welding was provided by a Model 9202 multi-range programmable DC power supply (B&K Precision, Yorba Linda, CA), capable of delivering up to 60 V/15 A/360 W [56].

Specifically for PLA samples welded with Ni—Co metal alloy mesh, an initial pressure of 2 MPa was applied, followed by a simultaneous pressure reduction to maintain a 2 mm displacement. In contrast, for samples using Ni—Cu mesh, we reduced the initial pressure after its application to slow down the displacement rate, accommodating for the melting of the polymer in the bonding area. The actual voltage, current, and power output for the welding were regulated and monitored using LabVIEW 2019 software. We programmed a ramp heating setting to avoid high current spikes and ensure a steady, uniform heat distribution across the metal mesh.

The experimental setup for resistance welding is shown in Fig. 4. A combination of micrographs is also shown for checking the bonding quality. Fig. 4 illustrates the resistance welding setup used for PLA samples, alongside micrographs of the bonding region at varying magnifications. These micrographs offer a detailed view of the bonding quality. Notably, no voids are observed between the metal wires and the PLA matrix, indicating a high-quality bond. However, Fig. 4b reveals a non-uniform interface, which can be attributed to the inherent waviness of the metallic mesh. This waviness, while affecting the uniformity, does not detract from the overall effectiveness of the bond. The results collectively demonstrate that the displacement resistance welding process is a viable technique for additive manufactured polymer structures. It successfully achieves a flat and uniform bonding area, which is crucial for the structural integrity and performance of these polymer-based assemblies.

The pressure-controlled resistance welding process was conducted on the additive manufactured polymer beams, shown in Fig. 5. Although this process is often adopted as a high-quality welding process for fiber-reinforced thermoplastic composites, the thermoplastic polymer structures are not compatible with this welding technique due to difficulty in controlling the process.

The pressure-controlled resistance welding process, as depicted in Fig. 5, was applied to additive manufactured polymer beams for comparative analysis with those fabricated using the displacement-controlled resistance welding process. Despite its widespread recognition as a high-quality method for welding fiber-reinforced thermoplastic composites, this technique proved less compatible with thermoplastic polymer structures due to challenges in controlling the process. In our experiment, the pressure was set at 0.5 MPa, with varying output voltage settings (1.5 V to 2.3 V) and resistance welding times (30s to 90s). The current limit was maintained at 15 A, using a 34 %/0.07 mm Ni—Cu metal alloy mesh as the heating element.

As observed in Fig. 5, the application of this method led to an overflow of polymer material when the interface region's temperature exceeded the glass transition temperature of the PLA beams. This resulted in misalignment issues between the welded parts. Although constant pressure-controlled resistance welding is a well-established method for thermoplastic matrix composites, it falls short in achieving satisfactory bonding quality with 3D printed polymer structures. Our investigation suggests that the displacement-controlled resistance welding process is more effective for fusion joining thermoplastic polymers, providing better control and overall bonding quality.

2.4. Three-point bending tests

Following ASTM D790 standard [57], we measured the flexural properties of the slender beam samples. The samples, measuring 152.40 × 76.20 × 14.68 mm, were subjected to three-point bending tests with a support span-to-depth ratio of 11:1. To investigate the effect of different infill patterns, three samples for each infill type were printed and tested. These tests aimed to identify the best structural performance, comparing these samples against continuously printed, smooth counterparts.

According to ASTM D790, the calculations for flexural stress, strain, strength, and modulus are given by Eqs. (1) to (4). In these equations, L, b, and d represent the specimen's support span length, width, and thickness, respectively. P denotes the midpoint span load, while P_{max} is the maximum load recorded by the Instron machine system. D refers to the mid-point deflection. σ_{f1}, σ_{f2} and $\varepsilon_{f1}, \varepsilon_{f2}$ are the stress and strain values at two points on the linear portion of the flexural stress-strain curve.

For the tests examining infill pattern effects, the crosshead speed was set between 4 and 6 mm/min. For measuring short beam flexural properties, we used a crosshead speed of 2 mm/min.

$$\sigma_f = 3PL/2bd^2 \tag{1}$$

$$\varepsilon_f = 6Dd/L^2 \tag{2}$$

$$\sigma_{f,max} = 3P_{max}L/2bd^2 \tag{3}$$

$$E_f = \left(\sigma_{f2} - \sigma_{f1}\right)/\left(\varepsilon_{f2} - \varepsilon_{f1}\right) \tag{4}$$

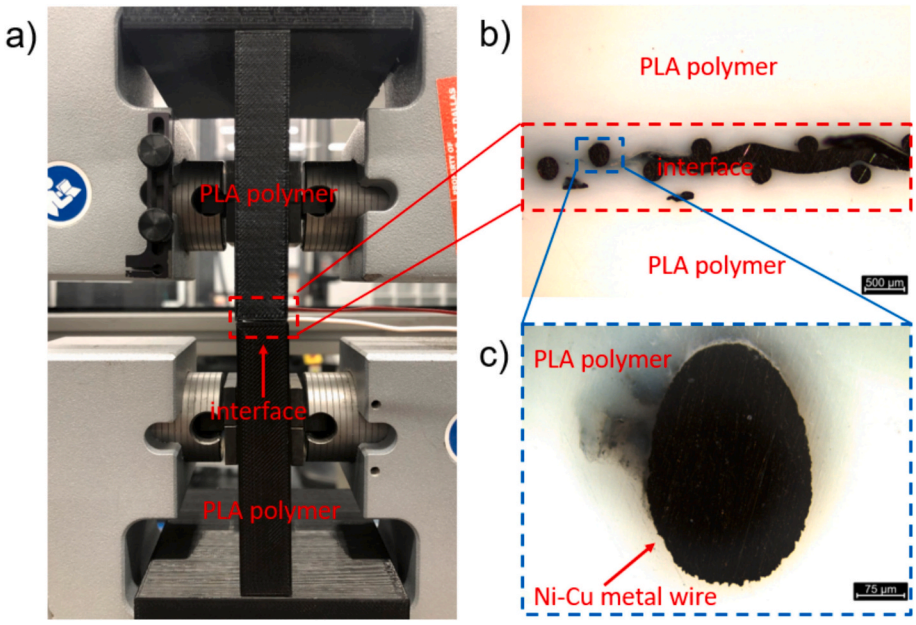

Fig. 4. Resistance welding experimental setup and microscopic analysis. a) Shows the 3D printed PLA polymer blocks secured in gripping fixtures on the Instron machine, ready for the resistance welding process; b) presents a 5× magnification micrograph of the resistance welding region, highlighting the detailed bonding area; c) displays a 20× magnification micrograph of the same region, offering a closer view of the bonding quality at a higher magnification.

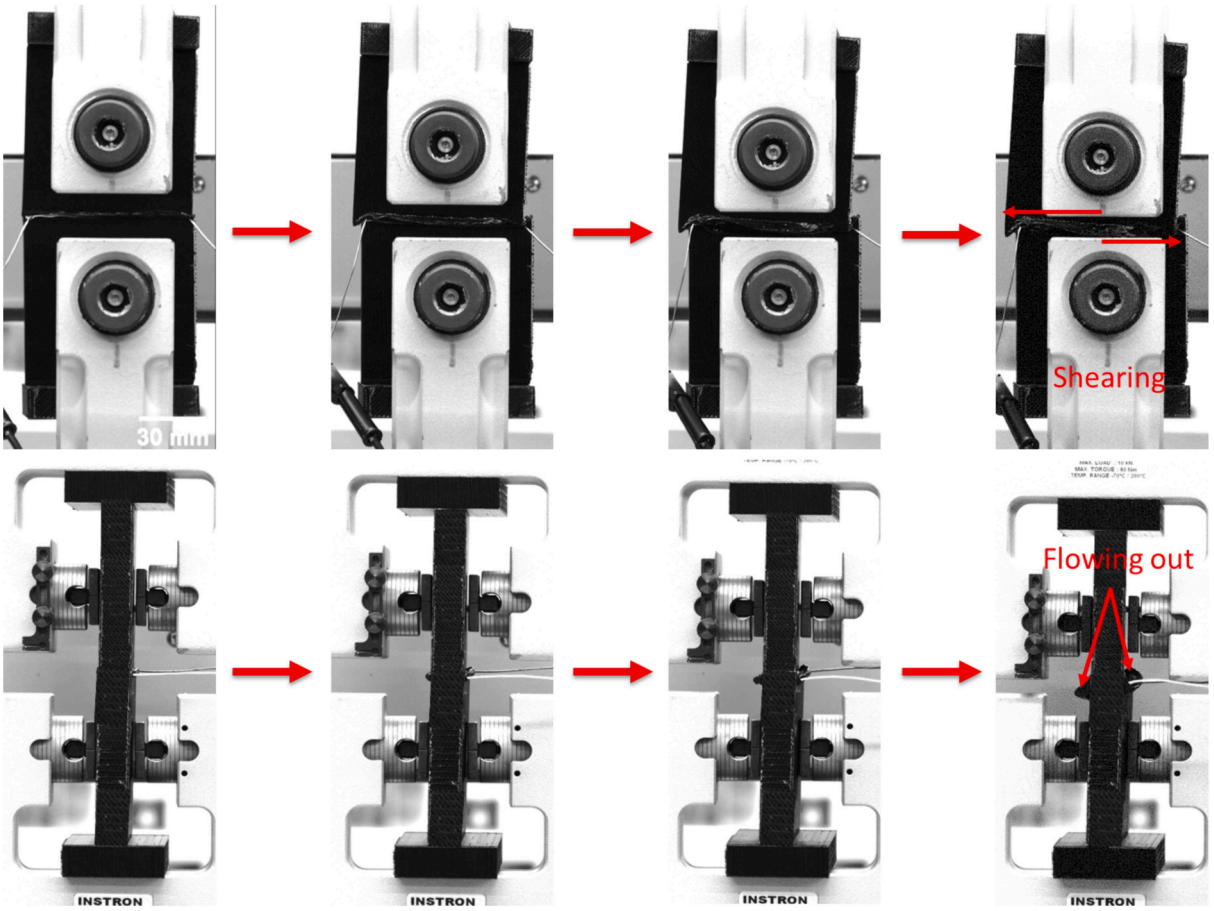

Fig. 5. Constant pressure-controlled resistance welded PLA slender beams under various welding time frames. This figure illustrates the effects of different welding durations on the PLA beams. From left to right, the beams were welded for 150 s, 180 s, 210 s, and 240 s, respectively. The top row shows the front view of each sample, demonstrating the overall alignment and bonding quality, while the bottom row presents the side view, highlighting the degree of polymer overflow and joint integrity.

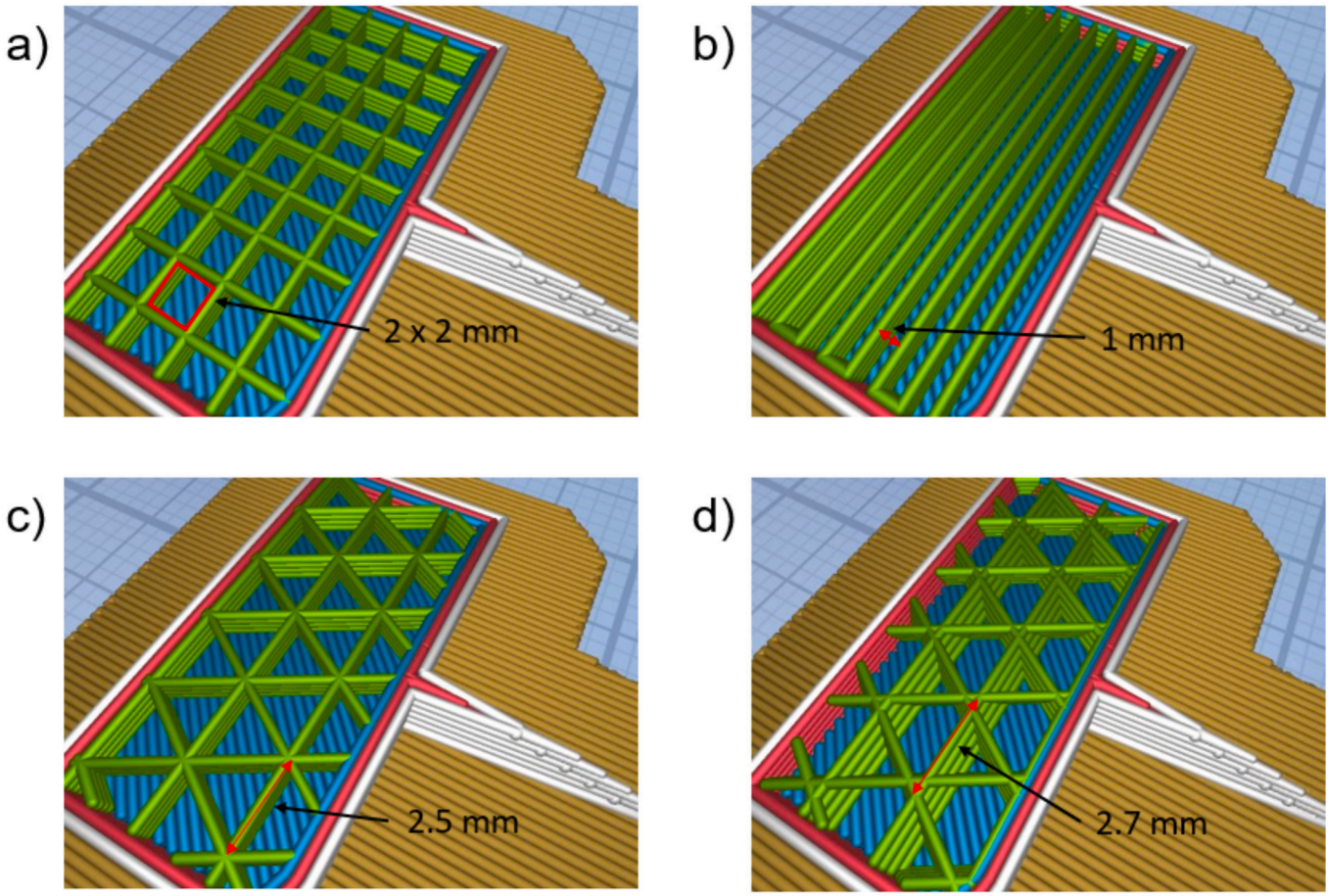

Fig. 6. Infill patterns of PLA samples (dimensions: 152.40 × 25.40 × 6.35 mm). This figure illustrates the four different infill patterns used in the PLA samples, each with an infill density of 40 %. a) Square infill pattern, featuring unit infilled squares of 2 × 2 mm; b) parallel infill pattern, with a spacing of 1 mm between two parallel infilled walls; c) 2D triangular infill pattern, where each unit infilled 2D triangle has edge dimensions of 2.5 × 2.5 × 2.5 mm; d) 3D triangular infill pattern, with each unit infilled 3D triangle having edge dimensions of 2.7 × 2.7 × 2.7 mm.

2.5. Digital image correlation (DIC) for surface strain measurement

The digital image correlation (DIC) technique [58,59], a non-contact method for measuring full-field deformations, was utilized to measure the side surface deformations of the specimens. We employed the 2D GOM Correlate software (GOM Inc., Charlotte, NC) for this purpose. During the three-point bending tests, a Nikon D7100 camera, equipped with a 24 mm lens and capable of capturing images at a resolution of 3840 × 2748 pixels, was used to record the specimen surface. Images were taken every second to accurately track deformation over time.

The camera was positioned at a work distance of 1.3 m, allowing for the capture of the entire support span within the specimen's region of interest. This distance ensured comprehensive coverage of the deformation area during testing. To ensure optimal visibility and image clarity, a NiLA VARSA LED light provided consistent illumination throughout the experiment.

3. Results and discussion

3.1. Mechanical characterization for the effect of infill patterns

In the material extrusion process of 3D printing, several factors such as infill pattern, infill density, layer height, printing temperature, and printing speed are crucial in determining the structural performance, weight, and cost of the sample [60]. For our samples, we opted for a 0.3 mm layer thickness. This choice was made to smooth the sample surface and minimize the voids between each layer and the printed filament. The infill density was set at 40 %, balancing rapid prototyping efficiency with maintaining adequate structural performance.

We explored four types of infill patterns to assess their effect on the sample's properties. These patterns included parallel lines, a square grid, a 2D-triangle grid, and a 3D-triangle grid. Fig. 6 provides an isometric view of these infill patterns, illustrating their different geometrical configurations.

Multiple infill patterns of the PLA samples flexural stress against flexural strain curves are shown in Fig. 7. A ductile type of failure is observed, and a similar bending stiffness is observed for all four types of infill patterns of PLA smooth beams. Across all four infill patterns, a ductile type of failure was universally observed, along with similar bending stiffness in the smooth PLA beams. As illustrated in Fig. 7a and b, the parallel and 3D-triangular infill patterns exhibited relatively higher ductility. Consistency across all four infill pattern structures was evident, indicated by the uniform linear elastic response observed in each case.

Interestingly, despite the brittle-type failure noted in Fig. 7c, all samples exhibited steady crack propagation. This behavior can be attributed to the internal lattice truss structure of the samples. Typically, cracks initiated near the indentation pin region on the outer layer, then propagated through the inner lattice truss, leading to necking, filament distortion, and eventually, filament breakage.

Table 2 provides a summary of the flexural strength and modulus for each infill pattern, all tested at the same infill density of 40 %. Among these, the 3D-triangle infill pattern demonstrated the highest flexural strength and modulus, surpassing the other three patterns. This result

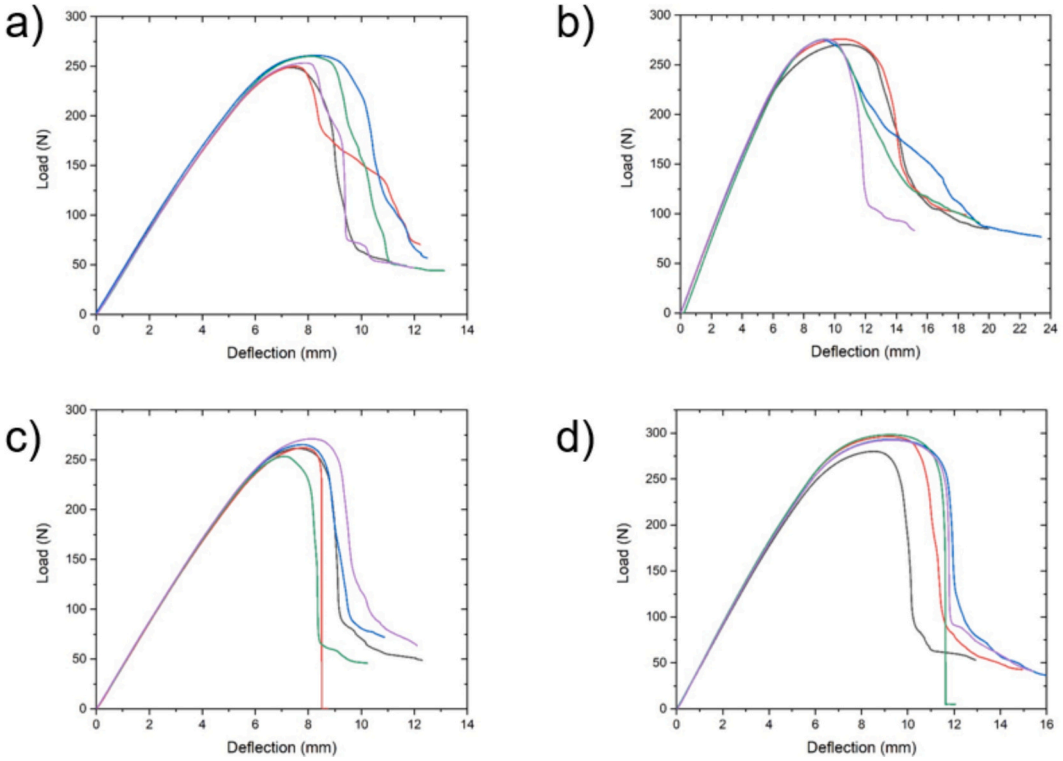

Fig. 7. Load-deflection curves for PLA samples with different infill patterns (dimensions: 152.40 × 25.40 × 6.35 mm). This figure shows the mechanical behavior of the PLA samples under load, each featuring a 40 % infill density but with varying infill patterns as shown in Fig. 6: a) Square infill pattern (Fig. 6a); b) parallel infill pattern (Fig. 6b); c) 2D triangular infill pattern (Fig. 6c); d) 3D triangular infill pattern (Fig. 6d). The curves illustrate the differences in load-bearing capacity and deflection characteristics attributable to each infill design.

Table 2
Flexural strength and flexural modulus of the PLA samples under four infill patterns.

Material	Infill type	Flexural strength (MPa)	Flexural modulus (GPa)	Specific flexural strength (MPa/(kg/m^3))	Specific flexural modulus (MPa/(kg/m^3))
PLA	40 % square	37.44 ± 0.71	1.72 ± 0.02	0.10 ± 0.002	4.65 ± 0.05
	40 % parallel	40.87 ± 0.17	1.68 ± 0.04	0.11 ± 0.0005	4.54 ± 0.11
	40 % 2D triangle	38.97 ± 0.96	1.78 ± 0.01	0.11 ± 0.003	4.81 ± 0.03
	40 % 3D triangle	43.45 ± 0.92	1.90 ± 0.03	0.12 ± 0.002	5.14 ± 0.08

indicates that the 3D-triangular infill pattern not only offers superior mechanical properties but also achieves the maximum strength-to-weight ratio among the evaluated designs.

3.2. Optimization of the resistance welding parameters

In Fig. 8, the relationship between voltage, current, and power output over time is plotted for three types of metal meshes used in resistance welding. To avoid a sudden temperature increase at the interface, a constant-rate heating setting was adopted. The voltage and current settings were configured as follows: for preheating the 36 %/0.25 mm Co—Ni and 30 %/0.11 mm Ni—Cu metal meshes, we set them at 0.5 V/1 V & 15 A & 30 s/30 s, while for the 34 %/0.07 mm Ni—Cu metal mesh, the settings were 0.5 V/1.5 V & 15 A & 30 s/30 s. According to data from the Instron system, the *Co*—Ni and Ni—Cu meshes began softening the polymer at 1 V, whereas the Ni—Cu mesh required 1.5 V to start the softening process.

Observations from Fig. 8a to d indicate that the 34 %/0.07 mm Ni—Cu metal mesh has the highest wire resistance, as evidenced by the lowest current output at a consistent voltage of 0.5 V. Based on Ohm's law, this mesh should produce the lowest power at the same voltage output. The wire resistances for the 36 %/0.25 mm Co—Ni, 30 %/0.11 mm Ni—Cu, and 34 %/0.07 mm Ni—Cu meshes are 0.12 Ω, 0.11 Ω, and 0.26 Ω, respectively. Unsteady power output at high current levels was observed in Fig. 8.

Adjusting the peak current level and the welding time at this level is crucial for optimizing bonding quality. Therefore, the selection of the peak current level was informed by the homogeneity and temperature levels indicated in the infrared thermal contour plots.

We investigated the effect of welding time at peak current levels over two-time frames (90, 180 s and 60, 120 s), with a 30 s increment in each case on the print quality. At these peak current levels, the power output initially reaches a maximum value but then gradually decreases. This decrease is attributed to reduced wire resistance under high temperatures. Therefore, a ramp type of heating is preferred to achieve uniform heating and high energy generation efficiency. Particularly at high current levels, it is advisable to shorten the welding time and increase the voltage more frequently. This approach counters the effect of temperature on wire resistance, optimizing power usage efficiency and achieving a higher welding temperature quickly.

Fig. 8b and f demonstrates that the compression pressure level applied to the metal mesh significantly influences wire resistance. For instance, with the 36 %/0.25 mm Co—Ni metal mesh, we observed that the wire resistance increased from 0.12 Ω to 0.50 Ω when the compression pressure was raised from 2 MPa to 6 MPa. Similarly, for the 34 %/0.07 mm Ni—Cu metal mesh, the resistance increased from 0.22 Ω to 0.26 Ω as the compression changed from 0.5 MPa to 2 MPa. This indicates that beyond a compression level of 2 MPa, the wire resistance

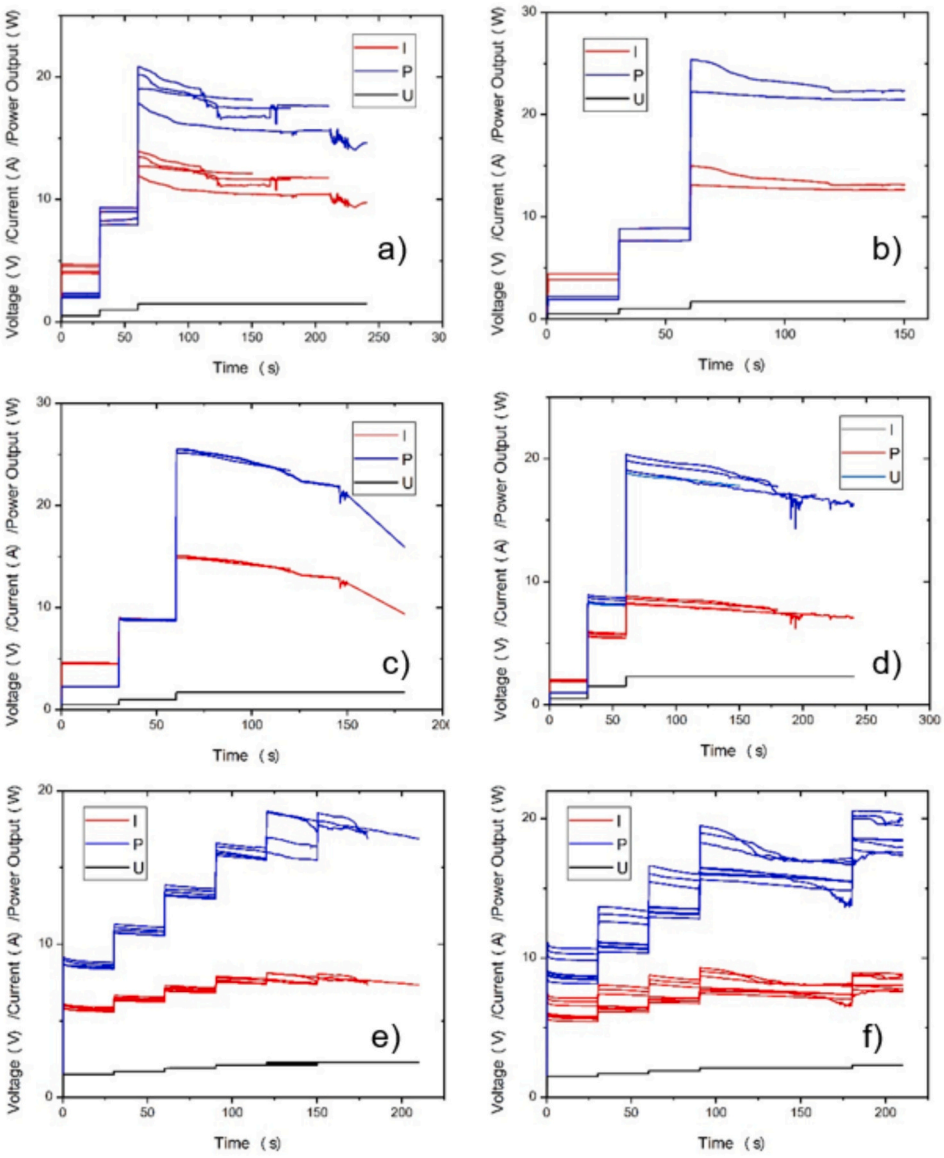

Fig. 8. Voltage (U), current (I), and power output (P) over resistance welding time with different metal meshes. This figure illustrates the electrical parameters during the resistance welding process for different metal mesh configurations: a) Ni-Co metal mesh under a 1.5 V voltage limit; b) Ni-Co metal mesh under a 1.7 V voltage limit; c) 30 %/0.11 mm Ni-Cu metal mesh under a 2.3 V voltage limit; d) 34 %/0.07 mm Ni-Cu metal mesh under a 1.7 V voltage limit; e) 34 %/0.07 mm Ni-Cu metal mesh under various voltage limits; f) 34 %/0.07 mm Ni-Cu metal mesh under combined 2.1 V & 2.3 V settings for 90 s & 30 s, respectively. (Note: The size of each metal mesh used in the experiments was 13.97 mm × 76.2 mm.)

change becomes more pronounced. Under a consistent current level, higher compression results in increased power efficiency.

Infrared thermal contour plots of metallic mesh were shown in Fig. 9. The heat distribution of the metal mesh was captured and the peak temperature generated at the center then gradually decreased to the surrounding. In Fig. 9, infrared thermal contour plots illustrate the heat distribution in metallic meshes during resistance welding. The plots show that the peak temperature typically originates at the center of the mesh and then decreases towards the surrounding areas. For this analysis, four settings that resulted in the best flexural response for each type of metal mesh were selected. Fig. 9a and b demonstrate that a temperature range of 95.4 °C to 110.1 °C is effective for melting the polymer using the 36 %/0.25 mm Ni—Co metal mesh (with an opening size of 0.381 mm). Likewise, Fig. 9c and d indicate that peak temperatures of 82.2 °C for the 30 %/0.11 mm Ni—Cu mesh (opening size: 0.14 mm) and 69.2 °C for the 34 %/0.07 mm Ni—Cu mesh (opening size: 0.07 mm) are adequate.

Observations from the infrared images reveal that when the current reaches 10 A or higher, electronic oscillations begin to occur, leading to a non-uniform and unsteady temperature distribution across the mesh. This effect underscores the need to adjust the peak welding temperature in accordance with the mesh's opening size. The larger the opening, the more power is required to effectively melt the polymer at these openings. Additionally, as the peak welding temperature increases, so does the thermal residual stress around the metal fibers. This increase is due to the larger temperature differential from room temperature, which has implications for the welding process's overall effectiveness.

Fig. 10 shows the loading history for a constant displacement rate compression approach using a 13.97 mm × 76.2 mm 34 %/0.07 mm Ni—Cu metal mesh. We explored four initial compression levels (0.25 MPa, 0.50 MPa, 2 MPa, and 4 MPa) to determine their role in polymer impregnation. Our results revealed that an initial compressive stress of 0.5 MPa optimally secures the polymer, avoiding overflow or interface voids. Additionally, three displacement rates (0.4 mm/min, 0.5 mm/

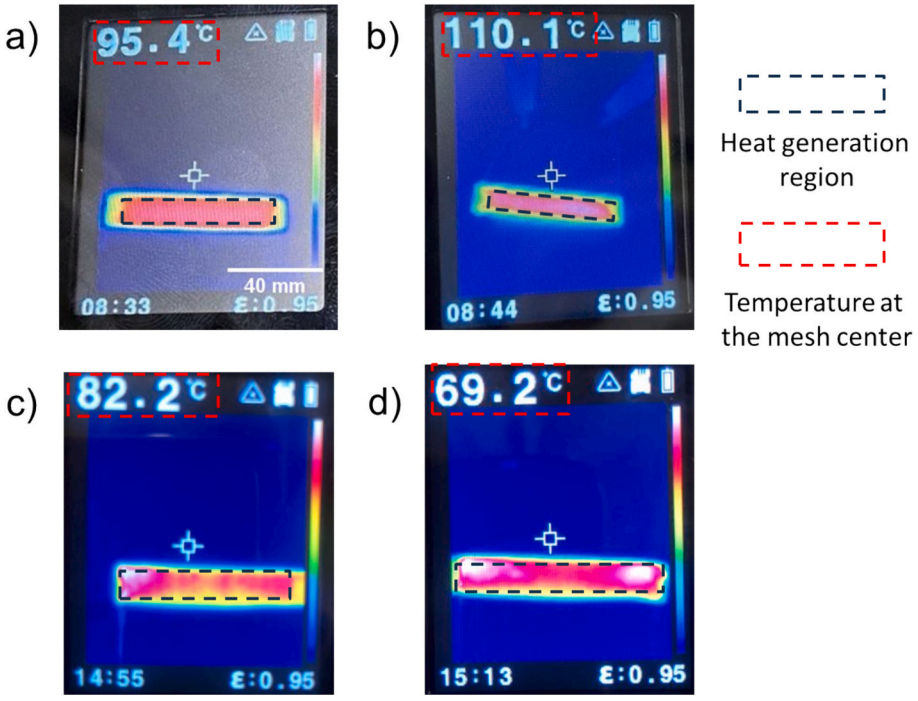

Fig. 9. Infrared thermal contour plot of metal meshes at peak temperature levels. This figure illustrates the temperature distribution in a 13.97 mm × 76.2 mm area of metal mesh under various ramp heating settings: a) 36 %/0.25 mm Ni-Co metal mesh with a 0.5 V/1 V/1.5 V voltage setting and a 30 s/30 s/150 s time frame; b) 36 %/0.25 mm Ni-Co metal mesh under 0.5 V/1 V/1.7 V voltage setting and 30 s/30 s/90 s time frame; c) 30 %/0.11 mm Ni-Cu metal mesh under 0.5 V/1 V/1.7 V voltage setting and 30 s/30 s/90 s time frame; d) 34 %/0.07 mm Ni-Cu metal mesh with a 1.5 V/1.7 V/1.9 V/2.1 V/2.3 V voltage setting and a 30 s/30 s/30 s/90 s/30 s time frame. (Note: Measurements were taken using a handheld infrared camera.)

min, and 0.6 mm/min) combined with two travel displacements (2 mm and 3 mm) were tested to find the best impregnation settings.

Interestingly, except for the setting with a 4 MPa initial compressive pressure, all twelve loading curves exhibited two peaks. The first peak corresponds to compression compaction and thermal expansion. As the polymer at the interface begins to soften and impregnate into the metal mesh, a load drop is observed. Under our constant displacement rate, this indicates that the rate of polymer softening exceeds the displacement rate. After reaching a certain displacement, especially in the 2 MPa initial compression setting, the rate of load drop slows down. In contrast, for the 0.5 MPa and 0.25 MPa settings, the load stops dropping and rises to a second peak. This second peak is attributed to the rate of thermal expansion in the polymer interface region outpacing the rate of polymer softening. Furthermore, a lower displacement rate under the same initial compression tends to exhibit higher thermal expansion.

Upon reaching the second peak, polymer melting, and squeeze flow commence, causing the load to sharply drop to 10–20 N. During certain intervals, the polymer slightly touches the compression platens. As the process concludes, the load draws back, and consolidation occurs until the crosshead stops at the predefined displacement level. Specifically, from Fig. 10c, the Ni/Cu, 2_6, Ni/Cu, 2_7, and Ni/Cu, 2_9 settings are projected to induce mechanical residual stresses of 1.25 MPa, 2 MPa, and 0.37 MPa, respectively. This is because the temperature of the polymer at the interface remains above its glass transition temperature (around 60 °C), while the crosshead continues to apply compression.

Fig. 11 shows a scatter plot comparing the average power output to the total energy consumption for three different types of metal meshes. One key observation is that the average power density tends to increase as the temperature on the metal mesh region rises, which in turn reduces wire resistance. Conversely, thermal oxidation on the metal mesh surface can lead to an increase in wire resistance, resulting in a decrease in average power density. According to Ohm's Law, with a constant current, there is a positive correlation between the increase of wire resistance and power output.

Fig. 11 shows a quadratic fit for the fixed voltage and current output across two time intervals and various metal meshes, with corresponding polynomial fit parameters listed in Table 3. We observed that as the welding time increases, the average power output initially rises and then decreases. This trend is attributed to the decreasing wire resistance over time. Further analysis, in conjunction with data from Fig. 9, reveals that higher peak temperatures lead to a more rapid drop in wire resistance. Specifically, the peak average power densities for the 30 %/0.11 mm Ni—Cu, 36 %/0.25 mm Co—Ni, and 34 %/0.07 mm Ni—Cu metal meshes are 15,757.32 W/m^2, 14,824.81 W/m^2, and 13,561.01 W/m^2, respectively, corresponding to peak welding temperatures of 82.2 °C, 95.4 °C, and 69.2 °C.

When the voltage, current, and welding time are fixed, a lower initial compression force on the metal mesh results in decreased wire resistance, thereby increasing power output. According to Joule's Law, lower wire resistance generates more energy when voltage is constant. This effect is also observed in Fig. 7f. While high wire resistance is preferable for low energy consumption and high efficiency, excessive compression force can compromise the polymer structure, leading to buckling due to the softening in the welding region. Considering structural integrity, a lower compression force is recommended for optimal resistance welding.

The relationships between power output, total generated energy, and compression forces follow a linear pattern. The parameters of this linear regression fit model, as listed in Table 3, indicate strong correlations with all R^2 values exceeding 90 %. This high R^2 value signifies a strong agreement between the polynomial fit curve and the scattered data points.

3.3. *The effect of resistance welding parameters and heating element type on the flexural properties*

Fig. 12 shows the load versus deflection curves for slender rectangular PLA beam samples (13.97 mm × 76.2 mm × 152.4 mm), which

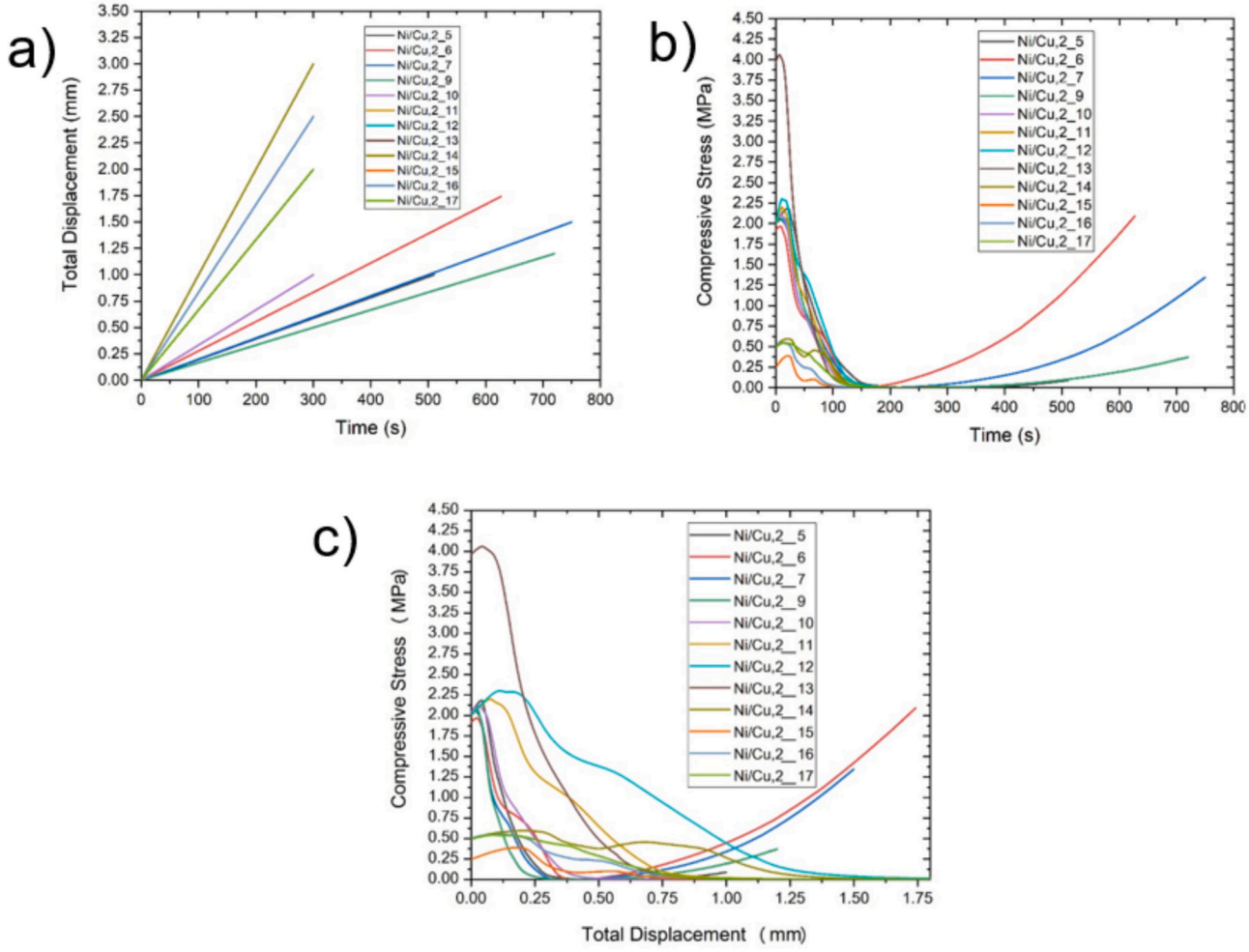

Fig. 10. Correlation between compressive stress, displacement, and resistance welding time in displacement-controlled resistance welding on a 13.97 mm × 76.2 mm 34 %/0.07 mm Ni-Cu metal mesh under varying initial compression pressures. It includes three key aspects: a) the total displacement of the mesh over time, highlighting the dynamics of the welding process; b) the compressive stress applied to the mesh over time, showing how stress evolves during welding; c) a direct comparison of compressive stress versus total displacement, demonstrating the mechanical behavior of the mesh under different welding conditions.

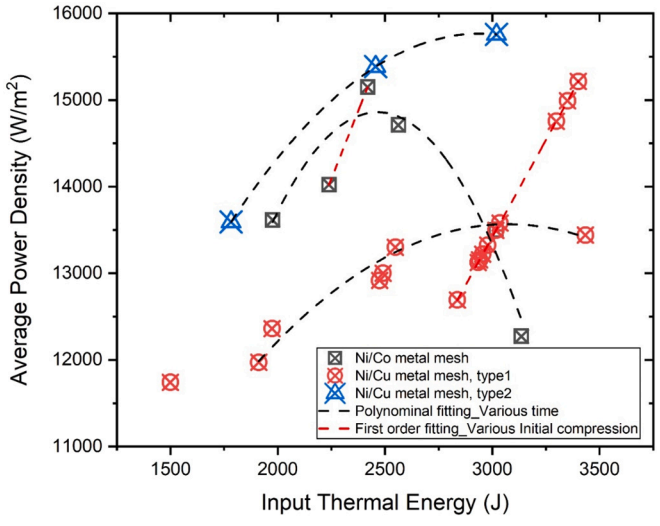

Fig. 11. Average power output versus total energy consumption, represented with a polynomial fit, for three distinct types of metal meshes. The plot helps to analyze how different mesh characteristics impact energy efficiency and power consumption in resistance welding.

illustrate the optimization process of resistance welding for three types of metal meshes. The best-optimized results are presented in Fig. 12a, b, and d. In Figs. 12a to 12c, dashed lines represent selected resistance welded PLA samples with good bonding quality, whereas in Fig. 12d, they indicate the smooth samples. Across all subfigures, the performance of the resistance welded PLA polymer slender beams is compared with that of smooth beams.

A key metric for assessing bonding quality is the peak load achieved by the samples. Higher peak loads indicate better bonding quality. Conversely, low flexural strength, flexural modulus, and maximum allowable strain (the flexural strain at the point of flexural strength) are indicative of poor quality. For instance, in Fig. 12a, the samples labeled 'Ni/Co, 1' and 'Ni/Co, 2' were set to the same power output but differed in their initial compressive stress (6 MPa and 2 MPa, respectively). The sample 'Ni/Co, 1' demonstrated superior bonding quality, attributed to its higher initial compressive stress level.

A high initial compressive stress in resistance welding does not necessarily result in an increased level of mechanical residual stress. According to data from the Instron system, the compressive stress for both 'Ni/Co, 1' and 'Ni/Co, 2' samples dropped to zero as the resistance welding process neared completion. This indicates that while a higher initial compressive stress improves bonding quality through enhanced polymer consolidation, it does not significantly affect residual stress levels.

Table 3
Second-order polynomial fit parameters for three metal mesh types. The meshes were tested under voltage limits of 1.5 V, 1.7 V, and 2.3 V across two sets of time intervals: 90 s, 120 s, 150 s, 180 s, and 60 s, 90 s, 120 s, respectively.

Material	Sample label	Polynomial equation	a	b	c	R^2 (%)
30 %/0.11 mm Ni-Cu metal alloy mesh/PLA matrix	Cu/Ni,1_1 to Cu/Ni,1_3	$y = ax^2 + bx + c$	−0.002	9.51	1776.02	100
34 %/0.07 mm Ni-Cu metal alloy mesh/PLA matrix	Cu/Ni,2_1 to Cu/Ni,2_4	$y = ax^2 + bx + c$	−0.001	7.20	2497.86	99.46
36 %/0.25 mm Co-Ni metal alloy mesh/PLA matrix	Co/Ni,3 to Co/Ni,6	$y = ax^2 + bx + c$	−0.005	27.07	−18,749.28	90.27
36 %/0.25 mm Co-Ni metal alloy mesh/PLA matrix	Co/Ni,1 and Co/Ni,2	$y = ax + b$	6.29	−0.11	–	100
34 %/0.07 mm Ni-Cu metal alloy mesh/PLA matrix	Cu/Ni,2_10 to Cu/Ni,2_17	$y = ax + b$	4.47	−0.02	–	100

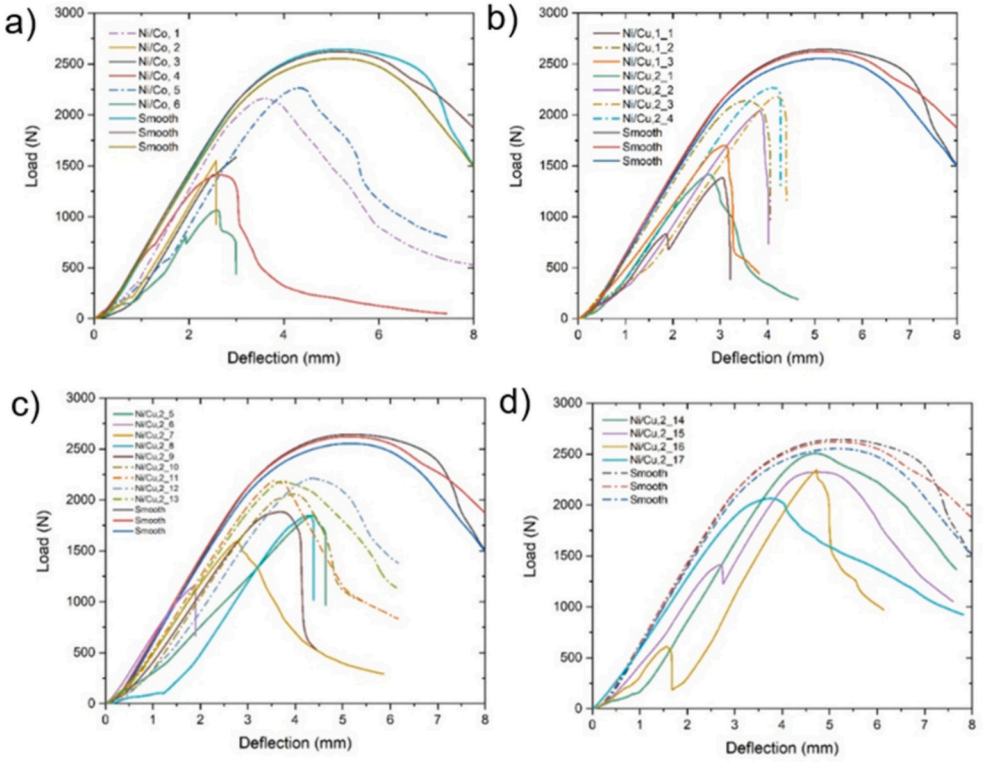

Fig. 12. The slender rectangular PLA beam samples (13.97 mm × 76.2 mm × 152.4 mm) load against deflection curves: a) resistance welded by the 36 %/0.25 mm Ni/Co metal mesh; b) resistance welded by the 30 %/0.11 mm Ni/Cu metal mesh; c) resistance welded by 34 %/0.07 mm Ni/Cu metal mesh under a constant displacement rate; d) resistance welded by 34 %/0.07 mm Ni/Cu metal mesh under a constant displacement rate and low compressive stress level.

Table 4
A summary of the resistance welding parameters, power efficiency, and flexural properties of the smooth beam and slender beam resistance welded by the 36 %/0.25 mm Co-Ni metal mesh.

Material	PLA Infill type	Thermal welding area (mm)	Sample label	Initially applied compression (MPa)	AC power voltage setting (V)	AC power current setting (A)	Thermal welding time (s)	Average power density (W/m2)	Total energy (J)	Flexural modulus (MPa)	Flexural Strength (MPa)	Maximum allowable strain (%)
36 %/0.25 mm Co-Ni metal alloy mesh/ PLA matrix	40 % 3D-triangle	13.97 mm × 76.2 mm	Ni/Co,1	6	0.5/1/1.7	15	30/30/90	14,021.48	2238.91	1073.73	22.14	2.9
			Ni/Co,2	2	0.5/1/1.7	15	30/30/90	15,148.20	2418.82	975.50	15.88	2.1
			Ni/Co,3	2	0.5/1/1.5	15	30/30/90	13,615.23	1976.40	1001.97	16.24	2.4
			Ni/Co,4	2	0.5/1/1.5	15	30/30/120	14,711.65	2562.67	880.07	14.41	2.2
			Ni/Co,5	2	0.5/1/1.5	15	30/30/150	13,499.25	3017.73	1008.18	23.21	3.6
			Ni/Co,6	2	0.5/1/1.5	15	30/30/180	12,272.19	3135.34	830.86	10.90	2.1
–	–	–	Smooth	–	–	–	–	–	–	1001.75 ± 21.51	26.70 ± 0.48	4.3

Table 5
A summary of the resistance welding parameters, power efficiency, and flexural properties of the smooth beam and slender beam resistance welded by the Co-Ni metal mesh.

Material	PLA infill type	Thermal welding area (mm)	Sample label	Initially applied compression (MPa)	Compression rate (mm/*min*)	Total displacement (mm)	AC power voltage setting (V)	AC power current setting (A)	Thermal welding time (s)	Average power density (W/m2)	Total energy (J)	Flexural modulus (MPa)	Flexural strength (MPa)	Maximum allowable strain (%)
30 %/0.11 mm Ni-Cu metal alloy mesh/PLA matrix	40 % 3D-triangle	13.97 mm × 76.2 mm	Cu/Ni,1_1	2	–	–	0.5/1/1.7	15	30/30/60	13,592.14	1782.27	731.97	14.18	2.5
			Cu/Ni,1_2	2	–	–	0.5/1/1.7	15	30/30/90	15,385.93	2456.78	960.48	21.91	2.9
			Cu/Ni,1_3	2	–	–	0.5/1/1.7	15	30/30/120	15,757.32	3019.30	792.16	17.42	2.5
34 %/0.07 mm Ni-Cu metal alloy mesh/PLA matrix	40 % 3D-triangle	13.97 mm × 76.2 mm	Cu/Ni,2_1	2	–	–	0.5/1.5/2.3	15	30/30/90	11,971.91	1911.64	721.49	14.50	2.3
			Cu/Ni,2_2	2	–	–	0.5/1.5/2.3	15	30/30/120	13,300.07	2548.46	907.40	20.93	3.1
			Cu/Ni,2_3	2	–	–	0.5/1.5/2.3	15	30/30/150	13,495.63	3016.92	866.46	22.34	3.5
			Cu/Ni,2_4	2	–	–	0.5/1.5/2.3	15	30/30/180	13,441.23	3434.01	922.00	23.24	3.4
			Cu/Ni,2_5	2	0.1176	1	1.5/1.7/1.9/2.1/2.3	15	30/30/30/30/90	13,580.93	3035.99	624.47	18.94	3.6
			Cu/Ni,2_6	2	0.1667	2	1.5/1.7/1.9/2.1	15	30/30/30/30	11,741.51	1499.88	656.22	11.79	1.5
			Cu/Ni,2_7	2	0.12	1.5	1.5/1.7/1.9/2.1/2.3	15	30/30/30/30/30	12,361.76	1973.89	877.23	16.32	2.3
			Cu/Ni,2_8	0	–	–	1.5/1.7/1.9/2.1/2.2/2.3	15	30/30/30/30/30/30	12,917.06	2475.07	580.46	18.90	3.5
			Cu/Ni,2_9	2	0.1	1.2	1.5/1.7/1.9/2.1/2.3	15	30/30/30/60/30	13,000.82	2491.12	863.27	19.29	3
			Cu/Ni,2_10	2	0.2	1	1.5/1.7/1.9/2.1/2.3	15	30/30/30/90/30	13,125.60	2934.20	909.85	21.08	3.3
			Cu/Ni,2_11	2	0.4	2	1.5/1.7/1.9/2.1/2.3	15	30/30/30/90/30	13,324.75	2978.72	934.05	22.43	2.9
			Cu/Ni,2_12	2	0.6	3	1.5/1.7/1.9/2.1/2.3	15	30/30/30/90/30	13,154.99	2940.77	766.85	22.67	3.5
			Cu/Ni,2_13	4	0.4	2	1.5/1.7/1.9/2.1/2.3	15	30/30/30/90/30	13,221.73	2955.69	894.96	22.38	3.0
			Cu/Ni,2_14	0.5	0.6	3	1.5/1.7/1.9/2.1/2.3	15	30/30/30/90/30	14,754.64	3298.37	944.02	25.68	3.8
			Cu/Ni,2_15	0.25	0.5	2	1.5/1.7/1.9/2.1/2.3	15	30/30/30/90/30	15,214.95	3401.27	813.99	23.80	3.8
			Cu/Ni,2_16	0.5	0.5	2.5	1.5/1.7/1.9/2.1/2.3	15	30/30/30/90/30	14,990.57	3351.11	849.35	24.03	3.8
			Cu/Ni,2_17	0.5	0.4	2	1.5/1.7/1.9/2.1/2.3	15	30/30/30/90/30	12,691.55	2837.17	847.10	21.14	3.1
PLA	–	–	Smooth	–	–	–	–	–	–	–	–	1001.75 ± 21.51	26.70 ± 0.48	4.3

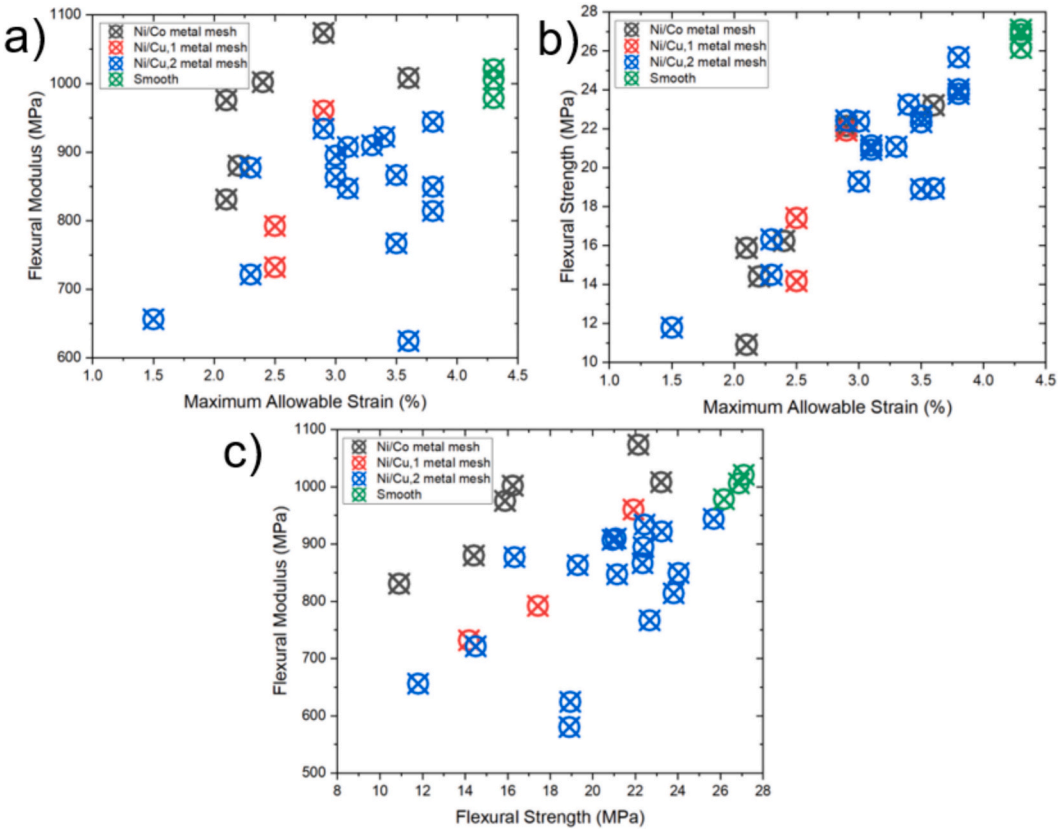

Fig. 13. Scatter plot of the flexural properties of the resistance welded and smooth PLA samples (13.97 mm × 76.2 mm × 152.4 mm): a) Flexural modulus against the maximum allowable strain; b) flexural strength against the maximum allowable strain; c) flexural modulus against the flexural strength.

Table 6
Mechanical properties of the 3D printed smooth beam and the slender beam bonded by the epoxy adhesive.

Material	Infill type	Sample label	Flexural strength (MPa)	Flexural modulus (MPa)	Maximum allowable strain (%)
PLA	40 % 3D-triangle	–	27.09	1020.79	4.3
		–	26.86	1006.05	4.3
		–	26.16	978.41	4.3
	Nominal Value	–	26.70 ± 0.48	1001.75 ± 21.51	–
PLA/ Plexus MA310	40 % 3D-triangle	–	17.74	942.82	2.7

For samples 'Ni/Co, 3' to 'Ni/Co, 6', the power output settings were consistent, but the resistance welding times at peak current levels varied (90 s, 120 s, 150 s, and 180 s). In Fig. 12b, samples 'Ni/Cu, 1_2', 'Ni/Cu, 2_3', and 'Ni/Cu, 2_4' are identified as having good bonding quality. Notably, 'Ni/Cu, 2_3' and 'Ni/Cu, 2_4' exhibit higher maximum allowable strains (3.5 % and 3.4 %, respectively) compared to 'Ni/Cu, 1_2' (2.9 %). This observation correlates with the findings from Fig. 9c and d, where a higher welding temperature at the peak current level was associated with a lower maximum allowable strain. The reasoning is that under a constant cooling rate, higher temperatures induce more thermal residual stress between the metal fiber and polymer matrix at the interface region.

In Fig. 12a and b, it is observed that the flexural strength of resistance welded PLA slender beams still falls short of that achieved by smooth PLA beams. To address this, we employed a displacement rate-controlled welding approach preceded by initial compression to enhance bonding quality. This process involved systematic modifications of several key parameters: displacement rate, total displacement, resistance welding time, and power output settings. We implemented a ramp heating setting with 0.2 V increments to increase the homogeneity of heat distribution [61], which is crucial for consistent bonding.

Particular attention was paid to the resistance welding time at the peak current levels of 2.3 V (first highest) and 2.1 V (second highest). Adjusting these times was essential for achieving optimal impregnation of the PLA polymer into the metal mesh. Moreover, we fine-tuned the displacement rate to improve polymer consolidation quality, while controlling total displacement was crucial to prevent the polymer from being over-squeezed out of the interface region. Over-squeezing, resulting from improper displacement settings, can cause polymer to spread around the interface region and onto the outer surface, potentially creating voids and compromising structural integrity [62].

Following these systematic modifications, samples labeled 'Ni/Cu, 2_10' to 'Ni/Cu, 2_13' were identified as exhibiting good bonding quality, demonstrating the effectiveness of our optimized welding parameters.

In Fig. 12c, it's observed that the peak load of the resistance welded PLA slender beams still does not match that of the smooth sample. This discrepancy is partly attributed to the high initial compressive stress, which causes the polymer to melt faster than the rate of displacement, leading to suboptimal polymer consolidation. To resolve this issue, we reduced the initial compressive pressure to 0.5 MPa and 0.25 MPa. The resulting load versus deflection curves for these modified settings are shown in Fig. 12d.

Among the resistance welded samples, 'Cu/Ni, 2_14' demonstrated the highest flexural strength at 25.68 MPa. Its flexural modulus and maximum allowable strain were measured at 944.02 MPa and 3.8 %, respectively. For comparison, the smooth sample exhibited a flexural strength of 26.70 ± 0.48 MPa, a flexural modulus of 1001.75 ± 21.51

Table 7
The bonding quality of the slender beam resistance welded by the metal mesh and bonded with epoxy adhesive. (Note: 1. Percentile data = mechanical properties of resistance welded beams/mechanical properties of slender beams; 2. bonding quality: >90 % is A, 80 %–89.99 % is B, 70 %–79.99 % is C. Rest percentiles are considered as poor quality.)

Material	Infill type	Sample label	Welding strength efficiency (%)	Welding modulus efficiency (%)	Welding maximum allowable strain efficiency (%)
PLA/ Plexus MA310	40 % 3D-triangle	–	66 %	94 %	63 %
30 %/0.11 mm Ni-Cu metal alloy mesh/ PLA matrix	40 % 3D-triangle	Cu/ Ni,1_1	53 %	73 %	58 %
		Cu/ Ni,1_2	82 %	96 %	67 %
		Cu/ Ni,1_3	65 %	79 %	58 %
34 %/0.07 mm Ni-Cu metal alloy mesh/ PLA matrix	40 % 3D-triangle	Cu/ Ni,2_1	54 %	72 %	53 %
		Cu/ Ni,2_2	78 %	91 %	72 %
		Cu/ Ni,2_3	84 %	86 %	81 %
		Cu/ Ni,2_4	87 %	92 %	79 %
		Cu/ Ni,2_5	71 %	62 %	84 %
		Cu/ Ni,2_6	44 %	66 %	35 %
		Cu/ Ni,2_7	61 %	88 %	53 %
		Cu/ Ni,2_8	71 %	58 %	81 %
		Cu/ Ni,2_9	72 %	86 %	70 %
		Cu/ Ni,2_10	79 %	91 %	77 %
		Cu/ Ni,2_11	84 %	93 %	67 %
		Cu/ Ni,2_12	85 %	77 %	81 %
		Cu/ Ni,2_13	84 %	89 %	70 %
		Cu/ Ni,2_14	96 %	94 %	88 %
		Cu/ Ni,2_15	89 %	81 %	88 %
		Cu/ Ni,2_16	90 %	85 %	88 %
		Cu/ Ni,2_17	79 %	85 %	72 %
36 %/0.25 mm Co-Ni metal alloy mesh/ PLA matrix	40 % 3D-triangle	Ni/Co,1	83 %	107 %	67 %
		Ni/Co,2	59 %	97 %	49 %
		Ni/Co,3	61 %	100 %	56 %
		Ni/Co,4	54 %	88 %	51 %
		Ni/Co,5	87 %	101 %	84 %
		Ni/Co,6	41 %	83 %	49 %

MPa, and a maximum allowable strain of 4.3 %. Thus, 'Cu/Ni, 2_14' represents the best bonding quality among the welded samples, reaching very closely to the mechanical performance of the smooth samples.

A comprehensive summary of the resistance welding parameters, along with the flexural and thermal properties for the three types of metal meshes, is presented in Tables 4 and 5. The detailed data points are compiled in Tables 4 and 5. In terms of energy consumption and power generation efficiency, our findings suggest that metal meshes with a smaller opening size and higher wire resistance are preferable for optimal electricity usage. This is particularly important in resistance welding processes, which should operate at lower current levels to minimize electric oscillation and the risk of current leakage. Furthermore, based on the equation for wire resistance, lower wire diameters and higher wire resistivities are preferred for achieving desirable welding outcomes.

Table 8
Multivariable linear regression analysis on the relationship between the welding efficiency and displacement-controlled resistance welding parameters of resistance welded PLA beams by 34 %/0.07 mm Ni-Cu metal alloy mesh (note: 1. y: welding efficiency = mechanical properties of resistance welded beams/mechanical properties of slender beams (0–100 %, or higher), x_1: Initial applied compression (MPa), x_2: Compression rate (mm/min), x_3: Total displacement (mm); 2. Condition: Resistance welding voltage: 1.5/1.7/1.9/2.1/2.3 V, resistance welding current limit: 15 A, resistance welding time: 30/30/30/90/30 s).

y	Polynomial equation	A	B	C	D	R^2
Welding strength efficiency	$y = A + Bx_1 + Cx_2 + Dx_3$	0.725	−0.006	0.452	−0.028	76.74
Welding modulus efficiency	$y = A + Bx_1 + Cx_2 + Dx_3$	0.89	0.005	−0.070	$-5.73 * 10^{-4}$	7.10
Welding max allowable strain Efficiency	$y = A + Bx_1 + Cx_2 + Dx_3$	0.74	−0.036	0.348	−0.028	63.01

The scatter plot of the flexural properties of the resistance welded and smooth short beam PLA samples are shown in Fig. 13. In Fig. 13a and c, we observed that among all the resistance welded beams, those using Ni/Co metal mesh exhibited the highest flexural modulus, given the same levels of maximum allowable strain and flexural strength. This outcome is attributed to the adequate thermal residual stress generated between the metal fiber and polymer matrix during the resistance welding process. Several factors influence this level of thermal residual stress, including cooling rate, peak temperature, and the volume of the metal mesh [63].

In our experiments, the cooling rate remained almost constant as all welding operations were conducted at room temperature. The significant thermal residual stress observed is primarily due to the high temperatures reached at peak current levels and the use of a relatively large wire diameter. Previous research has shown that an appropriate amount of thermal residual stress can enhance structural integrity [63,64]. This is because the polymer matrix may not bond effectively with the metal fiber due to different curing mechanisms in the resin/fiber system. A suitable level of residual stress can create mechanical interlocking between the metal fiber and the matrix, thus achieving improved structural integrity. This finding aligns with our results.

Contrary to the suggestions by Dube et al. [45], which indicate that enlarging the ratio of opening fraction to wire diameter could significantly increase bonding quality, our investigation found that this ratio does not significantly affect the flexural modulus and strength. As shown in Fig. 13b, there is a linear correlation between flexural strength and maximum allowable strain.

Tables 6 and 7 list the flexural strength, flexural modulus, and maximum allowable strain for slender beam samples resistance welded with various metal meshes. These properties are benchmarked against those of smooth samples and expressed as a percentage. Additionally, the flexural properties of adhesive-bonded slender beams (using Plexus MA310) and smooth slender beams are included for comparison.

Initially, the adhesive bond is considered to exhibit poor bonding quality, as indicated by its low flexural strength and maximum allowable limit. Another type of poor bonding, as seen in Table 7 with samples like 'Cu/Ni, 2_5' and 'Cu/Ni, 2_8', is characterized by a low flexural modulus. As previously mentioned, the level of residual stress significantly influences structural stiffness, prompting further investigation into how to effectively modify thermal residual stress.

Notably, the sample 'Cu/Ni, 2_14' achieved 96 %, 94 %, and 88 % of

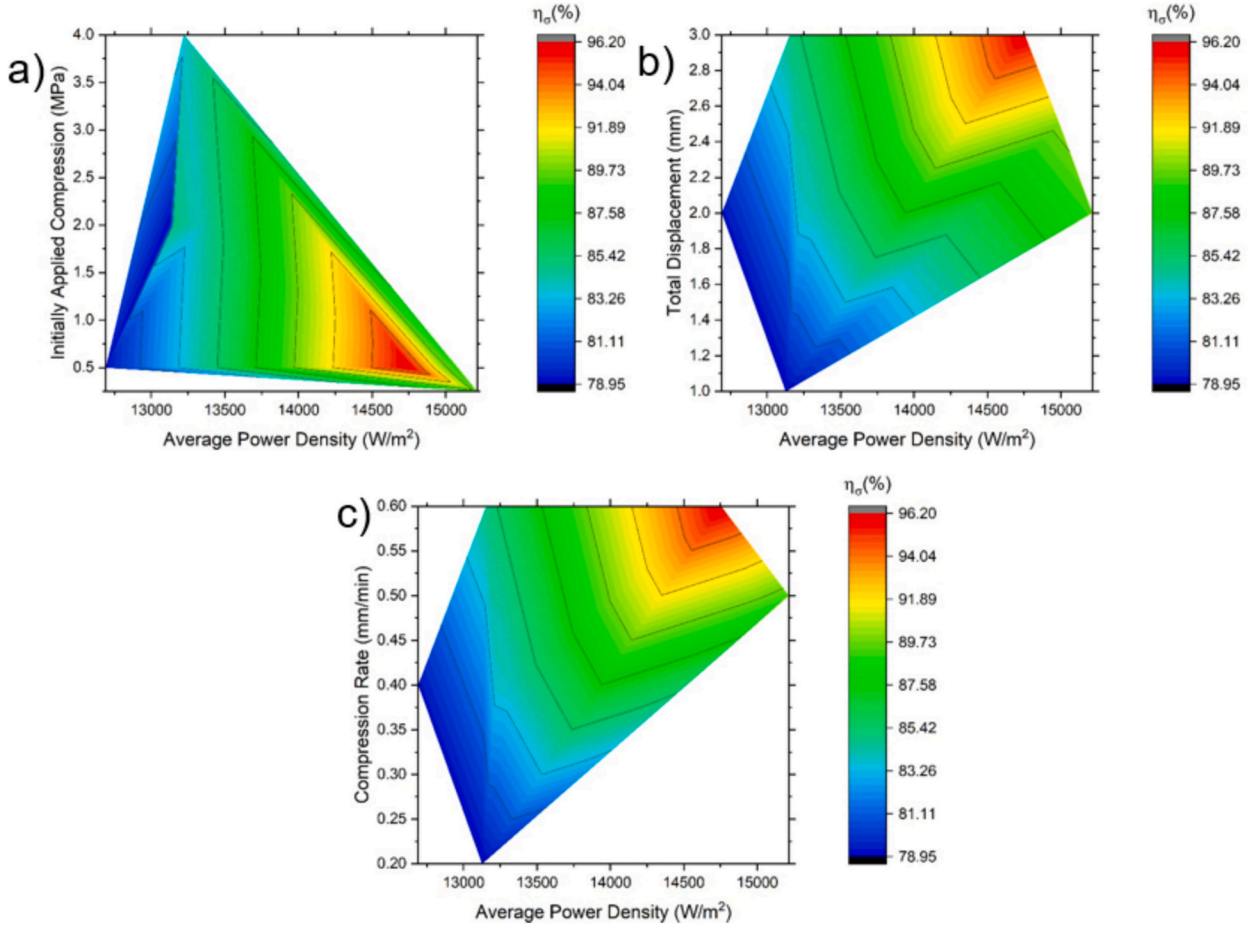

Fig. 14. 2D contour plot of welding strength efficiency, displacement-controlled resistance welding parameters, and resistance welding setup of resistance welded PLA beams by 34 %/0.07 mm Ni-Cu metal alloy mesh: a) welding strength efficiency against averaged power density and initially applied compression; b) welding strength efficiency against averaged power density and total displacement; c) welding strength efficiency against averaged power density and compression rate. (Note: Condition: Resistance welding voltage: 1.5/1.7/1.9/2.1/2.3 V, resistance welding current limit: 15 A, resistance welding time: 30/30/30/90/30 s.)

the smooth slender beams' flexural strength, modulus, and maximum allowable strain, respectively, marking it as the best bonding quality among all the samples tested. In contrast, while some samples welded with the 36 %/0.25 mm Co—Ni metal mesh surpassed the smooth sample in flexural modulus, they did not reach the same levels in flexural strength and maximum allowable strain.

Table 8 shows the relationship between displacement-controlled resistance welding efficiency and displacement-controlled resistance welding parameters. Based on the multivariable linear regression analysis, the displacement-controlled resistance welding parameters have a relatively strong relationship with the welding strength and maximum allowable strain efficiency ($R^2 > 50$ %), under a similar power setting (resistance welding time, voltage, and current). So, we are using the welding strength efficiency to show the effect of displacement-controlled resistance welding in Fig. 13. This also indicates that displacement-controlled resistance welding improves the strength more than improvements in the modulus.

Fig. 14 reveals that the most optimized process for welding PLA polymers using a 34 %/0.07 mm Ni—Cu metal alloy mesh involves certain specific conditions. An average power density between 14,500 and 14,800 W/m^2, a compression rate of 0.56 to 0.60 mm/min, a total displacement of 2.8 to 3.0 mm, and an initial compression of 0.5 to 1.1 MPa can achieve welding strength efficiencies >94 %. However, it is crucial to consider several sub-optimal scenarios identified during the process and their respective consequences.

As shown in Fig. 14a, an average power density around 13,000 W/m^2 leads to a discontinuous gradient and demonstrates that a higher initial compression increases welding strength efficiency. This effect is attributed to the enhancement of PLA polymer impregnation into the metal mesh during the early stages of resistance welding. While a lower average power density is more energy-efficient, a higher initial compression may cause local crushing or buckling issues. Consequently, when welding strength is comparable across different resistance welding plans, a lower initial compression is preferred.

When the PLA polymer achieves good impregnation (average power density at approximately 13,500 W/m^2), the initially applied compression becomes less critical compared to the compression rate and total displacement, up until the average power density reaches about 14,000 W/m^2. Fig. 14b and c indicates potential for further enhancing welding strength efficiency. However, caution is needed: an average power density exceeding 15,000 W/m^2 might lead to polymer deterioration at the interface, a compression rate higher than 0.6 mm/min can increase mechanical residual stress due to slower polymer melting and impregnation, and a total displacement above 3 mm could induce additional mechanical residual stress post-welding and squeeze out the liquid polymer, causing local buckling.

Herein, we investigated the relationship between the failure modes and welding parameters of the welded beams which shown in Fig. 15. Previous investigations have suggested a strong relationship between the failure modes of slender beams and their welding strength efficiency. Typically, the ranking of welding strength efficiency correlates with failure modes as follows: substrate failure > cohesive & substrate failure > adhesive & substrate failure > cohesive failure > adhesive failure [65,66]. However, as observed in Fig. 15a and b, in our study, the failure

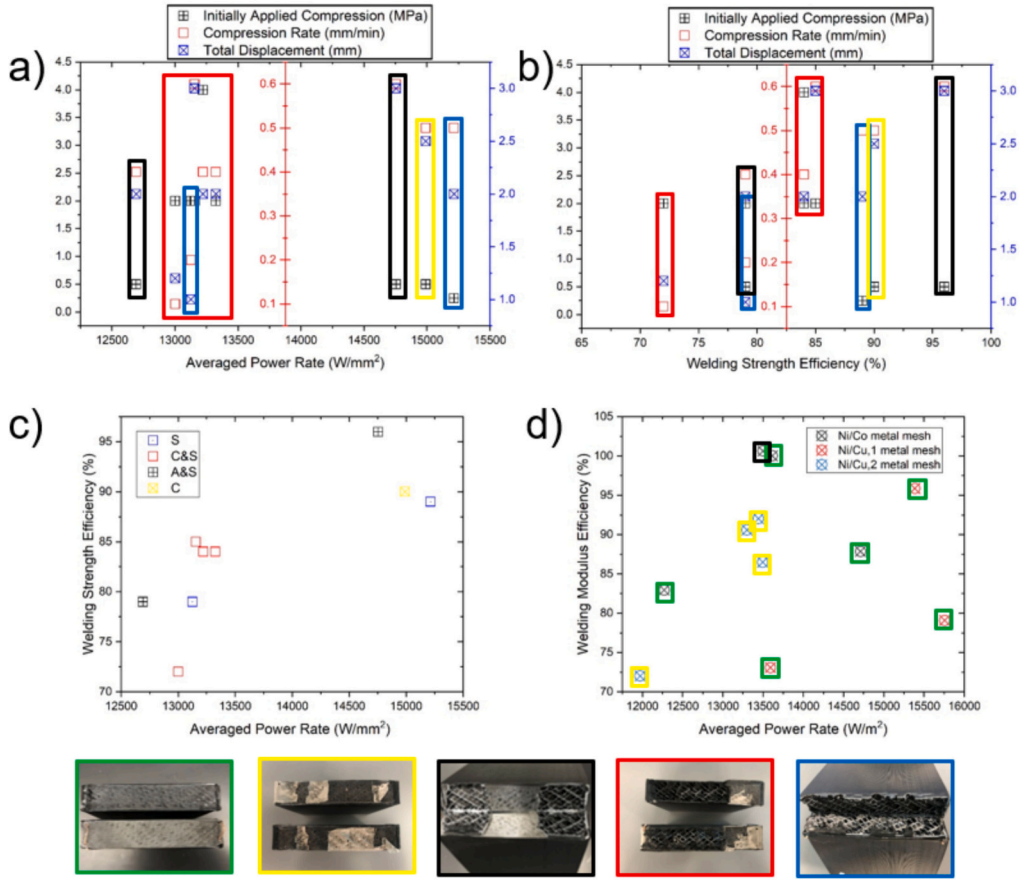

Fig. 15. Correlation between parameters of displacement-controlled resistance welding, averaged power rate, welding strength & modulus efficiency, and failure modes of the resistance welded PLA beams by three types of metal meshes; a) displacement-controlled resistance welding parameters versus averaged power rate; b) displacement-controlled resistance welding parameters versus welding strength efficiency; c) welding strength efficiency versus averaged power rate; d) welding modulus efficiency versus averaged power rate (note: Rectangular box zones under five colors are indicating the types of failure mode of displacement controlled resistance welded 3D printed beams under three-point bending: Substrate failure (S): blue; cohesive & substrate failure (C&S): red; adhesive & substrate failure (A&S): black; cohesive failure (C): yellow; adhesive failure (A): green). (For interpretation of the references to color in this figure legend, the reader is referred to the web version of this article.)

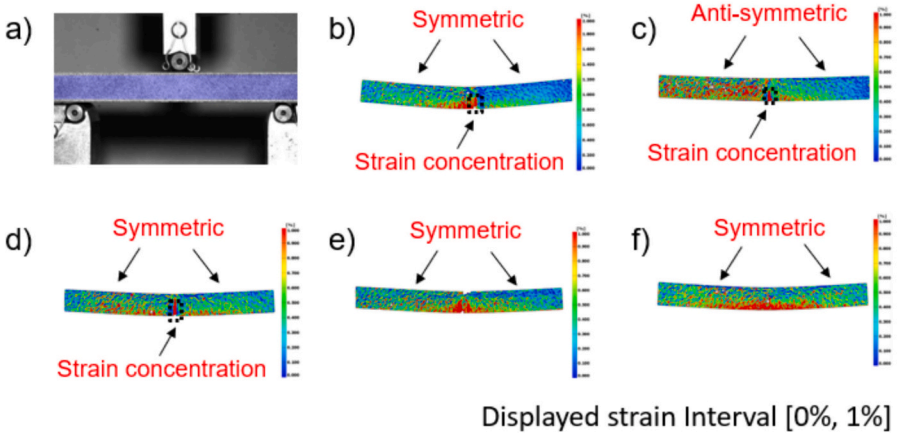

Fig. 16. Strain field in a slender beam under three-point bending as determined by digital image correlation (DIC): a) region of interest for the first principal strain measurements; b)–f) a contour plot of the first principal strain at the flexural strain of b): 7.44 % (beams resistance welded by 34 %/0.07 mm Ni-Cu metal mesh (Sample Ni/Cu, 2_14)); c): 3.84 % (beams resistance welded by 30 %/0.11 mm Ni-Cu metal mesh (Sample Ni/Cu, 1_2)); d): 4.22 % (beams resistance welded by 36 %/0.25 mm Co-Ni metal mesh); e): 4.30 % (beam adhesive-bonded by Plexus MA310); f): 3.74 % (smooth beam).

modes did not show a strong correlation with either the welding strength efficiency or the averaged power rate. While the general principles from previous studies are valid, in specific instances, the failure mode may not directly correspond to welding strength efficiency, possibly due to local defects, sample inconsistencies, or accidental fracture triggers.

Further analysis, detailed in Table 8, indicates that the parameters of

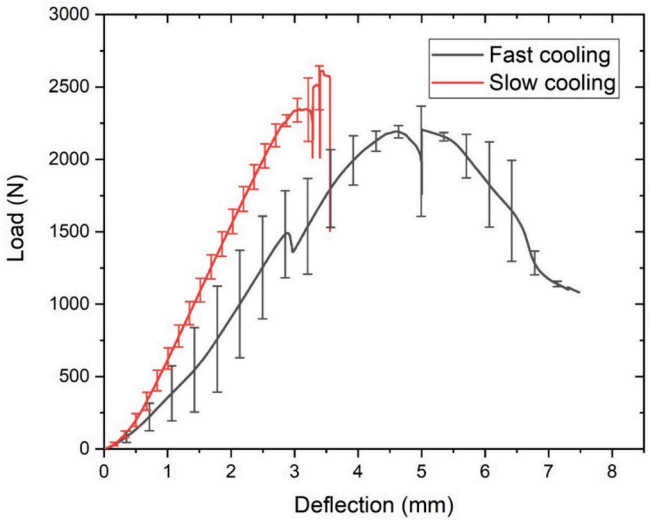

Fig. 17. Load versus deflection curves for the PLA slender beams resistance welded by 34 %/0.07 mm Ni-Cu metal mesh.

displacement-controlled resistance welding have a limited relationship with welding strength efficiency. We conducted an investigation focusing on modulus welding efficiency and the type of metal mesh used. Fig. 15d reveals interesting insights into the efficiency of different metal meshes. When comparing the 30 %/0.11 mm and 34 %/0.07 mm Ni—Cu metal alloy meshes, it was found that the 34 %/0.07 mm mesh requires approximately 14.8 % higher average power density to achieve a similar welding modulus efficiency. Conversely, the 36 %/0.25 mm Co—Ni metal alloy mesh demonstrates about 10 % higher welding modulus efficiency than the 34 %/0.07 mm Ni—Cu mesh under a comparable average power efficiency.

3.4. Surface strain distribution measured by 2D-DIC

Fig. 16 show the distribution of the first principal strains on the surface for resistance welded, adhesive bonded, and smooth slender beams. Utilizing Digital Image Correlation (DIC), we captured the strain at the middle-bottom point of slender beams under various conditions: resistance welded with 34 %/0.07 mm Ni—Cu metal mesh, 30 %/0.11 mm Ni—Cu metal mesh, 36 %/0.25 mm Co—Ni metal mesh, adhesive bonded, and smooth. This was conducted at a consistent time frame of 120 s to ensure a uniform level of curvature induced by the crosshead motion. The recorded strain values were 1.50 %, 7.05 %, 23.05 %, 2.47 %, and 2.32 %, respectively, for each type of beam.

The rationale behind selecting the same time frame for all beam types is to compare the strain fields under a similar bending condition. This comparison is vital for evaluating structural integrity by examining the level of strain concentration at the mid-bottom of the beams. This region is particularly critical as it is where the first fracture is likely to occur in a beam subjected to three-point bending. Through this analysis, we aim to determine which beam type is more susceptible to fracturing under similar stress conditions.

Through DIC observations, it is evident that the first principal strain primarily concentrates at the bonding region of the slender beams and then progressively extends outwards towards the two support ends. This strain pattern is particularly noticeable as the strain linearly increases from the top middle to the bottom side of the beam. This increase is attributed to a higher level of curvature present in the mid-bottom section of the beam, which is under more significant bending stress.

In Fig. 16c, an asymmetrical distribution of the first principal strain is observed, which can be linked to the uneven application of flexural loading and the anisotropic stiffness distribution within the bonding region. This asymmetry highlights the variation in mechanical response across different sections of the beam, indicating areas of potential weakness or heightened stress concentration. Understanding these strain patterns is crucial for assessing the structural integrity and performance of the beam under various loading conditions.

Overall, the investigation reveals that normal strain predominates in the smooth, resistance welded, and adhesive bonded slender beams, with no visible signs of residual stress in the smooth and adhesive bonded structures. In contrast, all resistance welded beams exhibit high surface strain concentration, attributable to thermal residual stress induced during the resistance welding process. This could adversely affect long-term performance, including aspects such as fatigue.

3.5. Effect of cooling rate on the resistance welded PLA slender beams

The effect of the cooling rate on the resistance-welded PLA slender beams is shown in Fig. 17. Two different cooling plans were chosen to modify the residual stress level in the interface region of the resistance-welded beams. The influence of cooling rate on resistance-welded PLA slender beams is depicted in Fig. 17. Two distinct cooling protocols were

Table 9
A comparison of joining strategies for the FDM printed thermoplastic polymer structures.

Reference	Substrate material	Implant material	Fusion joining process	Test method	Welding strength efficiency	Advantage	Disadvantage
Present study	PLA	34 %/0.07 mm Ni-Cu metal mesh	Displacement-controlled resistance welding	Three-point bending tests	79 %–96 %	Fast, easy setup, repeatable process	Current leakage, Proper implant material remain unclear
Poyraz et al. [67]	Polypropylene (PP)	Polypyrene nanogranule-coated carbon/catalyst	Ultrafast microwave welding	Lap shear tests	69.88 %–96.79 %	No need electrical connection, fast, no heat distortion	Hard to penetrate thick materials
Vijendra et al. [68]	Polyethylene (PE)	–	Induction heated tool-assisted friction-stir welding (I-FSW)	Tensile tests	77.11 %–104.32 %	Better bonding than FSW	Restricted to thin structure, surface damage, tedious setup, low hardness on the bonding area
Azhiri et al. [69]	ABS	Nano-silica	Friction stir welding (FSW)	Tensile tests	71 % (no nano-silica) 71 %–98 % (nano-silica)	Better bonding than FSW, high hardness on the bonding area	Restricted to thin structure, surface damage
Leicht et al. [70]	Polyarmide-12	Adhesive	Adhesive bonding	Lap shear tests	8 %–45 %	Fast, easy operation, good bonding surface finishing	Poor bonding quality
Balkan et al. [71]	PP/PE/PVC	Welding rod	Hot gas welding	Tensile tests	PE: 92.31 % PP: 77.27 % PVC: 76.92 %	Better bonding than FSW, high welding flexibility	Hard operation, poor surface finishing

employed to alter the residual stress levels in the interface region of these beams, with the resistance welding plan and heating element being the same as in the Ni/Cu, 2_14 sample. Post-welding, all six beams underwent a stress-relief process in a heating oven at 70 °C for 30 min. Subsequently, half of the samples were rapidly cooled in an ice water pool for 30 min, while the remaining three were allowed to cool slowly in the oven over 7 h, reaching room temperature. Following ASTM D790 standards, all samples underwent three-point bending tests. The data from Figs. 17 and 12d suggest that an optimal level of residual stress in the interface region is crucial for high-quality bonding in resistance-welded PLA beams, with the initial welds exhibiting superior performance. Variations in stiffness are primarily attributed to the annealing effect on the PLA polymer structure.

4. Discussion on the welding efficiency of displacement-controlled resistance welding process and future trend of fusion joining of additively-manufactured architecture

A detailed comparison between different joining strategies on the FDM-printed thermoplastic polymer structures is shown in Table 9. Compared with other joining methods, displacement-controlled resistance welding demonstrates commendable efficiency in achieving welding strength, as indicated by references [72,73]. Acherjee and Roudný et al. have suggested that an appropriate welding technique can be developed based on substrate stiffness [74,75]. This welding method offers numerous benefits. It is a rapid and straightforward process for bonding large polymer structures, requiring only a power source and electrical wires. Uniquely, it allows for embedding metal mesh and wires within the structure, ensuring strong internal bonding—an advantage not present in external joining processes. Additionally, displacement-controlled resistance welding maintains excellent surface finish, prevents damage at the bonding site, adheres to high geometric tolerances, and preserves the original 3D design from CAD software.

Despite its many advantages, displacement-resistance welding is not without limitations. It is a repeatable process, suitable for structural repairs, but these repairs are largely confined to surface or interface regions near the metal mesh. A significant drawback is the risk of current leakage due to the high voltage required for welding large areas, posing a safety hazard. Furthermore, the selection of suitable implant materials for this welding method is still a subject for further research.

Regarding other joining processes, friction stir welding can yield satisfactory bonding quality. However, this method often results in relatively low hardness and damage at the interface of the bonding region. Additionally, poor surface finishing is observed, attributed to the spinning action of the welding rod. In the case of microwave, ultrasonic, or induction welding, a major limitation is the difficulty in penetrating thick sample surfaces to reach the working area. Moreover, these methods can cause surface distortion due to residual energy remaining on the surface. Thus, each joining process has its own set of advantages and disadvantages. Determining which process is most effective for welding thermoplastic plastics in specific applications requires further investigation.

5. Conclusion

The bonding quality of slender PLA beams, joined through resistance welding and adhesive bonding, was examined using three-point bending tests and digital image correlation (DIC) experiments. For these experiments, three types of metal mesh—30 %/0.11 mm Ni—Cu, 34 %/0.07 mm Ni—Cu, and 36 %/0.25 mm Co-Ni—were chosen over stainless-steel mesh due to their lower current requirements, thereby maximizing power efficiency and ensuring safe operation. In line with previous findings, all three metal meshes demonstrated a high open area-to-wire diameter ratio, contributing to superior bonding quality. However, this ratio did not significantly affect the flexural strength and modulus of the beams. Microscopic examination of the resistance-welded samples revealed an absence of voids in the interface region, indicating effective bonding.

An investigation into the resistance welding process parameters revealed that factors such as power output, welding time, initial compressive pressure, displacement rate in the displacement-controlled process, and total displacement are crucial. Subsequently, comparisons were made between flexural strength, modulus, and maximum allowable strain of the welded beams and smooth slender PLA beams. It was found that a higher wire diameter coupled with a larger opening size results in an increased flexural modulus. For achieving high energy efficiency and safe operation in line with environmental sustainability and clean production goals, a metal mesh with small openings and high wire resistance is recommended. Conversely, for optimal structural performance characterized by high flexural stiffness, a metal mesh with a high wire diameter and large opening size is preferable. Both types of heating elements were shown to yield comparable results in terms of flexural strength and maximum allowable strain.

Multivariable linear regression analysis indicated that the displacement-controlled resistance welding process has a more pronounced effect on flexural strength than on modulus. Using a 34 %/0.07 mm Ni—Cu metal alloy mesh in the welding of PLA polymers, with parameters set to an average power density of 14,500 W/m^2, a compression rate of 0.60 mm/min, total displacement of 2.8 mm, and initial compression of 1.1 MPa, can achieve over 94 % (25.68 MPa) welding strength efficiency. Similarly, using 30 %/0.11 mm Ni—Cu and 36 %/0.25 mm Co—Ni meshes can optimize welding strength efficiencies to 82 % (21.91 MPa) and 87 % (23.21 MPa) respectively. Interestingly, the mode of failure does not significantly correlate with welding strength efficiency, which contrasts with previous findings on resistance welding.

Displacement-controlled resistance welding offers numerous benefits over other joining processes. While the optimal implant material is yet to be determined, Ni/Co or Ni/Cu metal meshes are preferred to stainless steel mesh due to their uniform heating distribution and safer welding characteristics. The use of PLA in engineering structures is particularly promising, offering several advantages over thermoset resin, notably in terms of additive manufacturability, recyclability, and reprocess-ability. Future investigations into displacement-controlled resistance welding should focus on its economic efficiency, sustainability, and potential for reducing environmental pollution, especially when applied to a wider range of composite materials or 3D-printed structures.

Declaration of competing interest

The authors declare that they have no known competing financial interests or personal relationships that could have appeared to influence the work reported in this paper.

Acknowledgments

We gratefully acknowledge the support of the National Science Foundation (NSF) under CMMI-2219347 and CMMI-1726435, from the NSF WindStar I/UCRC Center under IIP-1362033 and IIP-1916776, and from the Department of Energy (DoE) under DE-NA0003962 and DE-NA-0003525. Lu also thanks the support of the Louis Beecherl Jr. Chair. We would like also to thank Dr. Wei Li and Mr. Kishore M. Nagaraja for reviewing the manuscript.

References

[1] MacLeod M, Arp HPH, Tekman MB, Jahnke A. The global threat from plastic pollution. Science (80-). 2021;373(6550):61–65. doi:https://doi.org/10.1126/SCIENCE.ABG5433/ASSET/A6C792B7-8FA5-4DAC-8861-53C585B67DD2/ASSETS/GRAPHIC/373_61_F3.JPEG.

[2] Borrelle SB, Ringma J, Lavender Law K, et al. Predicted growth in plastic waste exceeds efforts to mitigate plastic pollution. Science (80-). 2020;369(6509):

1515–1518. doi:https://doi.org/10.1126/SCIENCE.ABA3656/SUPPL_FILE/ABA3656-BORRELLE-SM-DATA-S4.CSV.
[3] Di J, Reck BK, Miatto A, Graedel TE. United States plastics: large flows, short lifetimes, and negligible recycling. Resour Conserv Recycl 2021;167:105440. https://doi.org/10.1016/J.RESCONREC.2021.105440.
[4] Kazemi M, Faisal Kabir S, Fini EH. State of the art in recycling waste thermoplastics and thermosets and their applications in construction. Resour Conserv Recycl 2021;174:105776. https://doi.org/10.1016/J.RESCONREC.2021.105776.
[5] Ellis LD, Rorrer NA, Sullivan KP, et al. Chemical and biological catalysis for plastics recycling and upcycling. Nat Catal 2021 47. 2021;4(7):539–556. doi:https://doi.org/10.1038/s41929-021-00648-4.
[6] Ragaert K, Delva L, Van Geem K. Mechanical and chemical recycling of solid plastic waste. Waste Manag 2017;69:24–58. https://doi.org/10.1016/J.WASMAN.2017.07.044.
[7] Jehanno C, Alty JW, Roosen M, et al. Critical advances and future opportunities in upcycling commodity polymers. Nat 2022 6037903. 2022;603(7903):803–814. doi:https://doi.org/10.1038/s41586-021-04350-0.
[8] López-Fonseca R, Duque-Ingunza I, de Rivas B, Arnaiz S, Gutiérrez-Ortiz JI. Chemical recycling of post-consumer PET wastes by glycolysis in the presence of metal salts. Polym Degrad Stab 2010;95(6):1022–8. https://doi.org/10.1016/J.POLYMDEGRADSTAB.2010.03.007.
[9] Liu Y, Yao X, Yao H, et al. Degradation of poly(ethylene terephthalate) catalyzed by metal-free choline-based ionic liquids. Green Chem 2020;22(10):3122–31. https://doi.org/10.1039/D0GC00327A.
[10] Södergård A, Stolt M. Properties of lactic acid based polymers and their correlation with composition. Prog Polym Sci 2002;27(6):1123–63. https://doi.org/10.1016/S0079-6700(02)00012-6.
[11] Guo Y, Ji Z, Zhang Y, Wang X, Zhou F. Solvent-free and photocurable polyimide inks for 3D printing. J Mater Chem A 2017;5(31):16307–14. https://doi.org/10.1039/C7TA01952A.
[12] Pinto UA, Visconte LLY, Reis Nunes RC. Mechanical properties of thermoplastic polyurethane elastomers with mica and aluminum trihydrate. Eur Polym J 2001;37(9):1935–7. https://doi.org/10.1016/S0014-3057(01)00069-6.
[13] Ügdüler S, Van Geem KM, Denolf R, et al. Towards closed-loop recycling of multilayer and coloured PET plastic waste by alkaline hydrolysis. Green Chem 2020;22(16):5376–94. https://doi.org/10.1039/D0GC00894J.
[14] Bedell M, Brown M, Kiziltas A, Mielewski D, Mukerjee S, Tabor R. A case for closed-loop recycling of post-consumer PET for automotive foams. Waste Manag 2018;71:97–108. https://doi.org/10.1016/J.WASMAN.2017.10.021.
[15] Teotia M, Tarannum N, Soni RK. Depolymerization of PET waste to potentially applicable aromatic amides: their characterization and DFT study. J Appl Polym Sci 2017;134(31):45153. https://doi.org/10.1002/APP.45153.
[16] Rahimi M, Esfahanian M, Moradi M. Effect of reprocessing on shrinkage and mechanical properties of ABS and investigating the proper blend of virgin and recycled ABS in injection molding. J Mater Process Technol 2014;214(11):2359–65. https://doi.org/10.1016/J.JMATPROTEC.2014.04.028.
[17] Bai X, Isaac DH, Smith K. Reprocessing acrylonitrile-butadiene-styrene plastics: structure-property relationships. Polym Eng Sci 2007;47(2):120–30. https://doi.org/10.1002/PEN.20681.
[18] Su KH, Lin JH, Lin CC. Influence of reprocessing on the mechanical properties and structure of polyamide 6. J Mater Process Technol 2007;192-193:532–8. https://doi.org/10.1016/J.JMATPROTEC.2007.04.056.
[19] Suresh SS, Mohanty S, Nayak SK. Composition analysis and characterization of waste polyvinyl chloride (PVC) recovered from data cables. Waste Manag 2017;60:100–11. https://doi.org/10.1016/J.WASMAN.2016.08.033.
[20] Olifirov LK, Kaloshkin SD, Ergin KS, Tcherdyntsev VV, Danilov VD. Solid-state recycling of polyimide film waste. J Appl Polym Sci 2013;127(4):2960–8. https://doi.org/10.1002/APP.37964.
[21] Wölfel B, Seefried A, Allen V, Kaschta J, Holmes C, Schubert DW. Recycling and reprocessing of thermoplastic polyurethane materials towards nonwoven processing. Polym 2020, Vol 12, Page 1917. 2020;12(9):1917. doi:https://doi.org/10.3390/POLYM12091917.
[22] Abbasian M, Massoumi B, Mohammad-Rezaei R, Samadian H, Jaymand M. Scaffolding polymeric biomaterials: are naturally occurring biological macromolecules more appropriate for tissue engineering? Int J Biol Macromol 2019;134:673–94. https://doi.org/10.1016/J.IJBIOMAC.2019.04.197.
[23] Blok LG, Longana ML, Yu H, Woods BKS. An investigation into 3D printing of fibre reinforced thermoplastic composites. Addit Manuf 2018;22:176–86. https://doi.org/10.1016/J.ADDMA.2018.04.039.
[24] Mitchell A, Lafont U, Hołyńska M, Semprimoschnig C. Additive manufacturing — a review of 4D printing and future applications. Addit Manuf 2018;24:606–26. https://doi.org/10.1016/J.ADDMA.2018.10.038.
[25] Zhu G, Hou Y, Xu J, et al. Reprintable polymers for digital light processing 3D printing. Adv Funct Mater 2021;31(9):2007173. https://doi.org/10.1002/ADFM.202007173.
[26] Obande W, Ó Brádaigh CM, Ray D. Continuous fibre-reinforced thermoplastic acrylic-matrix composites prepared by liquid resin infusion – a review. Compos Part B Eng 2021;215:108771. https://doi.org/10.1016/J.COMPOSITESB.2021.108771.
[27] Cao D, Malakooti S, Kulkarni VN, Ren Y, Lu H. Nanoindentation measurement of core–skin interphase viscoelastic properties in a sandwich glass composite. Mech Time-Dependent Mater 2020. https://doi.org/10.1007/s11043-020-09448-y [Published online].
[28] Cao D, Malakooti S, Kulkarni VN, et al. The effect of resin uptake on the flexural properties of compression molded sandwich composites. Wind Energy July 20, 2021:we.2661. https://doi.org/10.1002/WE.2661 [Published online].
[29] Wang X, Xu T, Andrade MJ De, et al. The interfacial shear strength of carbon nanotube sheet modified carbon fiber composites. In: Challenges in Mechanics of Time-dependent Materials. Vol 2. Conference Proceedings of the Society for Experimental Mechanics Series; 2021. doi:https://doi.org/10.1007/978-3-030-59542-5_4.
[30] Deng S, Wu J, Dickey MD, et al. Rapid open-air digital light 3D printing of thermoplastic polymer. Adv Mater 2019;31(39):1903970. https://doi.org/10.1002/ADMA.201903970.
[31] Tiwary VK, P A, Malik VR. An overview on joining/welding as post-processing technique to circumvent the build volume limitation of an FDM-3D printer. Rapid Prototyp J 2021;27(4):808–21. https://doi.org/10.1108/RPJ-10-2020-0265/FULL/PDF.
[32] Li L, Tirado A, Nlebedim IC, et al. Big area additive manufacturing of high performance bonded NdFeB magnets. Sci Rep 2016;6(1):1–7. https://doi.org/10.1038/srep36212.
[33] Duty CE, Compton B, Post B, et al. Structure and mechanical behavior of Big Area Additive Manufacturing (BAAM) materials. Rapid Prototyp 2017. https://doi.org/10.1108/RPJ-12-2015-0183 [Published online].
[34] Mason H. UMaine composites center receives three Guinness World Records related to largest 3D printer, UMaine News - University of Maine. CompositesWorld; 2019. https://umaine.edu/news/blog/2019/10/10/umaine-composites-center-receives-three-guinness-world-records-related-to-largest-3d-printer/. [Accessed 17 December 2021].
[35] Li T, Wang L. Bending behavior of sandwich composite structures with tunable 3D-printed core materials. Compos Struct 2017;175:46–57. https://doi.org/10.1016/J.COMPSTRUCT.2017.05.001.
[36] Hou S, Li T, Jia Z, Wang L. Mechanical properties of sandwich composites with 3d-printed auxetic and non-auxetic lattice cores under low velocity impact. Mater Des 2018;160:1305–21. https://doi.org/10.1016/J.MATDES.2018.11.002.
[37] Tian X, Jin J, Yuan S, Chua CK, Tor SB, Zhou K. Emerging 3D-printed electrochemical energy storage devices: a critical review. Adv Energy Mater 2017;7(17):1700127. https://doi.org/10.1002/AENM.201700127.
[38] Yousefpour A, Hojjati M, Immarigeon J-P. Fusion bonding/welding of thermoplastic composites. J Thermoplast Compos Mater 2004;17(4):303–41. https://doi.org/10.1177/0892705704045187.
[39] Grujicic M, Sellappan V, Omar MA, et al. An overview of the polymer-to-metal direct-adhesion hybrid technologies for load-bearing automotive components. J Mater Process Technol 2008;197(1–3):363–73. https://doi.org/10.1016/J.JMATPROTEC.2007.06.058.
[40] Zhao S, Kimura F, Kadoya S, Kajihara Y. Experimental analysis on mechanical interlocking of metal–polymer direct joining. Precis Eng 2020;61:120–5. https://doi.org/10.1016/J.PRECISIONENG.2019.10.009.
[41] Ageorges C, Ye L, Hou M. Advances in fusion bonding techniques for joining thermoplastic matrix composites: a review. Compos - Part A Appl Sci Manuf 2001;32(6):839–57. https://doi.org/10.1016/S1359-835X(00)00166-4.
[42] ASTM International. ASTM D5868 - 01(2014) standard test method for lap shear adhesion for fiber reinforced plastic (FRP) bonding. https://www.astm.org/Standards/D5868. [Accessed 19 August 2021].
[43] Eveno EC, John W, Gillespie J. Resistance welding of graphite polyetheretherketone composites: an experimental investigation. J Thermoplast Compos Mater 2016;1(4):322–38. https://doi.org/10.1177/089270578800100402.
[44] Warren KC, Lopez-Anido RA, Freund AL, Dagher HJ. Resistance welding of glass fiber reinforced PET: effect of weld pressure and heating element geometry. J Reinf Plast Compos 2016;35(12):974–85. https://doi.org/10.1177/0731684416633516.
[45] Dubé M, Hubert P, Gallet JN, Stavrov D, Bersee HE, Yousefpour A. Metal mesh heating element size effect in resistance welding of thermoplastic composites: doi:101177/0021998311412986. 2011;46(8):911–919. doi:https://doi.org/10.1177/0021998311412986.
[46] Russello M, Catalanotti G, Hawkins SC, Falzon BG. Welding of thermoplastics by means of carbon-nanotube web. Compos Commun 2020;17:56–60. https://doi.org/10.1016/J.COCO.2019.11.001.
[47] Murray RE, Roadman J, Beach R. Fusion joining of thermoplastic composite wind turbine blades: lap-shear bond characterization. Renew Energy 2019;140:501–12. https://doi.org/10.1016/j.renene.2019.03.085.
[48] Roy Choudhury M, Debnath K. Improving the mechanical performance of resistance-welded green composite joints using different heating elements. Polym Test 2021;94:107059. https://doi.org/10.1016/J.POLYMERTESTING.2021.107059.
[49] Reis JP, Moura M de, Samborski S. Thermoplastic composites and their promising applications in joining and repair composites structures: a review. Mater 2020, Vol 13, Page 5832. 2020;13(24):5832. doi:https://doi.org/10.3390/MA13245832.
[50] Panneerselvam K, Aravindan S, Noorul Haq A. Study on resistance welding of glass fiber reinforced thermoplastic composites. Mater Des 2012;41:453–9. https://doi.org/10.1016/J.MATDES.2012.05.025.
[51] Rzeczkowski J, Samborski S, Valvo PS. Effect of stiffness matrices terms on delamination front shape in laminates with elastic couplings. Compos Struct 2020;233:111547. https://doi.org/10.1016/J.COMPSTRUCT.2019.111547.
[52] Rider AN, Wang CH, Cao J. Internal resistance heating for homogeneous curing of adhesively bonded repairs. Int J Adhes Adhes 2011;31(3):168–76. https://doi.org/10.1016/j.ijadhadh.2011.01.001.
[53] Shahrubudin N, Lee TC, Ramlan R. An overview on 3D printing technology: technological, materials, and applications. In: Procedia manufacturing. vol. 35. Elsevier B.V.; 2019. p. 1286–96. https://doi.org/10.1016/j.promfg.2019.06.089.
[54] McMaster-Carr. High-temperature nickel-chromium wire cloth. Accessed May 3, 2021. https://www.mcmaster.com/wire-cloth/material~nickel/.

[55] Craftbot. CraftBot3 user manual. Accessed May 3, 2021. https://support.craftbot.com/hc/en-us/articles/360006825077-Craftbot-3-User-Manual.
[56] B&K Precision. Model 9202, Multi-range programmable DC power supplies. Accessed May 4, 2021. https://www.bkprecision.com/products/power-supplies/9202-360w-multi-range-60v-15a-dc-power-supply.html.
[57] ASTM International. ASTM D790 - 17 standard test methods for flexural properties of unreinforced and reinforced plastics and electrical insulating materials. Published 2017. Accessed May 4, 2021. https://www.astm.org/Standards/D790.
[58] Vend Roux G, Knauss WG. Submicron deformation field measurements: part 2. Improved digital image correlation Exp Mech 1998;38(2):86–92. https://doi.org/10.1007/BF02321649.
[59] Lu H, Cary PD. Deformation measurements by digital image correlation: implementation of a second-order displacement gradient. Exp Mech 2000;40(4):393–400. https://doi.org/10.1007/BF02326485.
[60] Wang X, Jiang M, Zhou Z, Gou J, Hui D. 3D printing of polymer matrix composites: a review and prospective. Compos Part B Eng 2017;110:442–58. https://doi.org/10.1016/j.compositesb.2016.11.034.
[61] Ageorges C, Ye L, Hou M. Experimental investigation of the resistance welding for thermoplastic-matrix composites. Part I: heating element and heat transfer. Compos Sci Technol 2000;60(7):1027–39. https://doi.org/10.1016/S0266-3538(00)00005-1.
[62] Dubé M, Hubert P, Yousefpour A, Denault J. Resistance welding of thermoplastic composites skin/stringer joints. Compos Part A Appl Sci Manuf 2007;38(12):2541–52. https://doi.org/10.1016/J.COMPOSITESA.2007.07.014.
[63] Parlevliet PP, Bersee HEN, Beukers A. Residual stresses in thermoplastic composites - a study of the literature. Part III: effects of thermal residual stresses. Compos Part A Appl Sci Manuf 2007;38(6):1581–96. https://doi.org/10.1016/j.compositesa.2006.12.005.
[64] Hausmann J, Naghipour P, Schulze K. Analytical and numerical residual stress models for fiber metal laminates – comparison and application. Procedia Mater Sci 2013;2:68–73. https://doi.org/10.1016/J.MSPRO.2013.02.009.
[65] Xiong X, Wang D, Wei J, et al. Resistance welding technology of fiber reinforced polymer composites: a review. J Adhes Sci Technol 2021;35:1593–619. https://doi.org/10.1080/01694243.2020.1856514.
[66] Ageorges C, Ye L, Hou M. Advances in fusion bonding techniques for joining thermoplastic matrix composites: a review 2006;32:2001.
[67] Poyraz S, Zhang L, Schroder A, Zhang X. Ultrafast microwave welding/reinforcing approach at the interface of thermoplastic materials. ACS Appl Mater Interfaces 2015;7(40):22469–77. https://doi.org/10.1021/ACSAMI.5B06484/ASSET/IMAGES/AM-2015-064845_M001.GIF.
[68] Vijendra B, Sharma A. Induction heated tool assisted friction-stir welding (i-FSW): a novel hybrid process for joining of thermoplastics. J Manuf Process 2015;20:234–44. https://doi.org/10.1016/J.JMAPRO.2015.07.005.
[69] Azhiri RB, Mehdizad Tekiyeh R, Zeynali E, Ahmadnia M, Javidpour F. Measurement and evaluation of joint properties in friction stir welding of ABS sheets reinforced by nanosilica addition. Measurement 2018;127:198–204. https://doi.org/10.1016/J.MEASUREMENT.2018.05.005.
[70] Leicht H, Orf L, Hesselbach J, et al. Adhesive bonding of 3D-printed plastic components. doi:101080/0021846420191682561. 2019;96(1–4):48–63. doi: https://doi.org/10.1080/00218464.2019.1682561.
[71] Balkan O, Demirer H, Ezdeşir A, Yildirim H. Effects of welding procedures on mechanical and morphological properties of hot gas butt welded PE, PP, and PVC sheets. Polym Eng Sci 2008;48(4):732–46. https://doi.org/10.1002/PEN.21014.
[72] Liu Z, Li Y, Liu Z, Yang Y, Li Y, Luo Z. Ultrasonic welding of metal to fiber-reinforced thermoplastic composites: a review. J Manuf Process 2023;85:702–12. https://doi.org/10.1016/j.jmapro.2022.12.001.
[73] Xu X, Ren H, Chen S, Luo X, Zhao F, Xiong Y. Review on melt flow simulations for thermoplastics and their fiber reinforced composites in fused deposition modeling. J Manuf Process 2023;92:272–86. https://doi.org/10.1016/j.jmapro.2023.02.039.
[74] Acherjee B. Laser transmission welding of polymers – a review on process fundamentals, material attributes, weldability, and welding techniques. J Manuf Process 2020;60:227–46. https://doi.org/10.1016/j.jmapro.2020.10.017.
[75] Roudný P, Syrový T. Thermal conductive composites for FDM 3D printing: a review, opportunities and obstacles, future directions. J Manuf Process 2022;83:667–77. https://doi.org/10.1016/j.jmapro.2022.09.026.